Science Advances
AAAS

Supplementary Materials for

Preempting fermion sign problem: Unveiling quantum criticality through nonequilibrium dynamics in imaginary time

Yin-Kai Yu *et al.*

Corresponding author: Shuai Yin, yinsh6@mail.sysu.edu.cn; Zi-Xiang Li, zixiangli@iphy.ac.cn

Sci. Adv. **12**, eadz4856 (2026)
DOI: 10.1126/sciadv.adz4856

This PDF file includes:

Sections S1 to S4
Figs. S1 to S19
Tables S1 to S5
References

S1. DETAILS OF NONEQUILIBRIUM IMAGINARY-TIME DYNAMICS IN PQMC SIMULATION

A. Imaginary-time relaxation dynamics simulated by PQMC

We focus on the imaginary-time relaxation dynamics from a fully ordered or Dirac semimetal initial state $|\psi_0\rangle$. The initial state is prepared by solving $H_0|\psi_0\rangle = E_0|\psi_0\rangle$, where H_0 is the initial Hamiltonian and E_0 is the ground state energy. With these initial states, the evolution of the observable $O(\tau)$ is given by

$$\langle O(\tau)\rangle = \frac{\langle\psi_0|\,\mathrm{e}^{-\frac{\tau}{2}H}\;O\;\mathrm{e}^{-\frac{\tau}{2}H}\,|\psi_0\rangle}{\langle\psi_0|\,\mathrm{e}^{-\tau H}\,|\psi_0\rangle}. \tag{S1}$$

As $\tau\to\infty$, $\mathrm{e}^{-\frac{\tau}{2}H}$ projects the system onto the ground state of H.

The imaginary-time relaxation dynamics can be simulated via the projector quantum Monte Carlo (PQMC) (51, 53, 54). In conventional PQMC studies, a sufficiently large τ (usually τ should be several times as large as L) is needed to ensure that the ground state is obtained. Then the physical qualities are calculated in the ground state.

In contrast, in our work, we focus on the short-time stage of the imaginary-time relaxation process, where τ does not need to be large compared to L. In this regime, the system remains in a nonequilibrium state rather than the ground state This stage is usually discarded in conventional PQMC studies. In our previous work, we systematically and carefully investigated the imaginary-time nonequilibrium dynamics of Dirac fermion systems (50), and found that although this setup goes beyond the conventional PQMC framework, choosing a small τ only introduces some dependence on the initial state, while the ground-state information, particularly universal quantum criticality, still manifests in the nonequilibrium dynamics. With a properly chosen initial state, one can fix τ/L^z to a small value and still observe quantum phase transitions via standard finite-size scaling analysis, even in this nonequilibrium regime.

A similar practice has also appeared earlier in the context of finite-temperature QMC (FTQMC). In FTQMC, the expectation value of an observable is given by $\langle O\rangle = \frac{1}{Z}\mathrm{Tr}[\mathrm{e}^{-\beta(H-\mu N)}O]$, with $Z = \mathrm{Tr}[\mathrm{e}^{-\beta(H-\mu N)}]$ (5, 6, 75). Here, $\beta = 1/k_{\mathrm{B}}T$ is the inverse temperature, and it corresponds to the imaginary-time extent in the Monte Carlo simulation. Unlike zero-temperature PQMC, FTQMC involves both quantum and thermal fluctuations. When FTQMC is used to study zero-temperature quantum phase transitions, it is common to fix β/L^z to a finite value (typically $\beta = L^z$) to obtain temperature-independent finite-size scaling. There are also studies using smaller values, such as $\beta = \frac{1}{4}L^z$ (76).

Although both β and τ represent the imaginary-time length in QMC simulations, they carry distinct physical meanings. A shorter β in FTQMC corresponds to a higher-temperature thermal equilibrium state, and it is widely accepted that β/L^z can be used as a dimensionless scaling factor. In contrast, a shorter τ in zero-temperature PQMC corresponds to a nonequilibrium state and has rarely been considered outside the context of imaginary-time nonequilibrium dynamics (49, 50, 77). Here, based on our understanding of imaginary-time nonequilibrium dynamics, we leverage this idea to address the fermion sign problem in zero-temperature PQMC simulation. Moreover, compared to conventional PQMC and FTQMC approaches, our framework further alleviates the sign problem by flexibly choosing appropriate initial states, while the consistency of results obtained from different initial states provides a useful means of self-consistency check.

B. Hubbard-Stratonovich transformation

In the PQMC simulations, the interaction terms in the form of four-fermion operators should be decoupled via Hubbard-Stratonovich (HS) transformation. The implementation of PQMC begins with performing the Trotter decomposition to discretize the imaginary-time evolution operator into $M = \tau/\Delta\tau$ (where M is an integer) time slices, i.e.,

$$\mathrm{e}^{-\tau H} = \prod_{m=1}^{M}\left[\mathrm{e}^{-\Delta\tau H_t}\mathrm{e}^{-\Delta\tau H_U} + \mathcal{O}\left(\Delta\tau^2\right)\right], \tag{S2}$$

where H_t and H_U represent the free fermion hopping term and the interaction term in the Hamiltonian, respectively. Then, we use the HS transformation on H_U to decouple the fermion-fermion interaction into interactions between non-interacting fermions and auxiliary fields.

For the single-Dirac-fermion Hubbard model, we use the following HS transformation:

$$\mathrm{e}^{-\Delta\tau U\left(n_{i\uparrow}-\frac{1}{2}\right)\left(n_{i\downarrow}-\frac{1}{2}\right)} = \frac{1}{2}\mathrm{e}^{-\frac{\Delta\tau U}{4}}\sum_{s_i=\pm1}\mathrm{e}^{\lambda s_i\left(c_{i\uparrow}^{\dagger}c_{i\downarrow}+c_{i\downarrow}^{\dagger}c_{i\uparrow}\right)}. \tag{S3}$$

where $\cosh\lambda = \mathrm{e}^{\frac{\Delta\tau U}{2}}$. For $U > 0$ (Hubbard repulsive interaction), the sign problem arises for all channels. We here choose the σ_x channel to mitigate the sign problem (55). This choice also affects the structure of the fermion determinant. Specifically, due to the spin-flipping nature of the free-fermion hopping term in the single-Dirac-fermion Hubbard model, the σ_x-channel decoupling leads to an auxiliary-field Hamiltonian that only has off-diagonal blocks. As a result, the total fermion determinant can be factorized into the product of two smaller determinants: $\det(M) \propto \det(M_{\uparrow\downarrow})\det(M_{\downarrow\uparrow})$. In contrast, decoupling in the σ_z channel does not permit this factorization. This results in a single determinant of twice the dimension, which typically exacerbates the sign problem.

For the spinless t-V model, previous studies have shown that at half-filling, the model can be decoupled into the hopping channel without the sign problem, which has been demonstrated from various perspectives (20, 21, 23, 24). In our study, however, we use the HS transformation in a sign-problematic channel, namely the density channel:

$$\mathrm{e}^{-\Delta\tau V\left(n_i-\frac{1}{2}\right)\left(n_j-\frac{1}{2}\right)} = \frac{1}{2}\mathrm{e}^{-\frac{\Delta\tau V}{4}}\sum_{s_{ij}=\pm1}\mathrm{e}^{\lambda s_{ij}(n_i-n_j)}. \tag{S4}$$

where $\cosh\lambda = \mathrm{e}^{\frac{\Delta\tau V}{2}}$. Despite the presence of sign problem, the numerical results we obtained are consistent with the previously established results, demonstrating the reliability of our new method.

For the SU(3) repulsive Hubbard model, we use the following HS transformation:

$$\mathrm{e}^{\Delta\tau\frac{U}{2}(n_{i\alpha}-n_{i\beta})^2} = \frac{1}{2}\sum_{s_i=\pm1}\mathrm{e}^{\lambda s_i(n_{i\alpha}-n_{i\beta})}. \tag{S5}$$

where $\cosh\lambda = \mathrm{e}^{\frac{\Delta\tau U}{2}}$. For all the known algorithms, the SU(3) repulsive Hubbard model is sign-problematic for any decoupling channel in HS transformation.

C. Sign problem in PQMC

Through the HS transformation, the Hamiltonian can be converted into a quadratic effective form of fermionic operators that depends on the spacetime configuration of the auxiliary fields. The partition function can then be expressed as a sum of configuration weight $w(\mathrm{c})$, i.e., $Z = \sum_{\mathrm{c}} w(\mathrm{c})$. These weights are given by the determinant of the effective Hamiltonian of fermions (51).

In PQMC simulations, we sample the space-time dependent configuration of the auxiliary field. For sign-free models, the sampling probability is proportional to the configuration weight $w(\mathrm{c})$. However, for the sign-problematic models, the configuration weight $w(\mathrm{c})$ is not positive definite, so it cannot be used directly as the sampling probability. Instead, the absolute value $|w(\mathrm{c})|$ is used as the sampling probability, and the observables are computed as follows (9, 15):

$$\langle O\rangle = \frac{\sum_{\mathrm{c}} w(\mathrm{c})O(\mathrm{c})}{\sum_{\mathrm{c}} w(\mathrm{c})} = \frac{\sum_{\mathrm{c}}|w(\mathrm{c})|\mathrm{sign}(\mathrm{c})O(\mathrm{c})/\sum_{\mathrm{c}}|w(\mathrm{c})|}{\sum_{\mathrm{c}}|w(\mathrm{c})|\mathrm{sign}(\mathrm{c})/\sum_{\mathrm{c}}|w(\mathrm{c})|} = \frac{\langle O\,\mathrm{sign}\rangle_{|w|}}{\langle\mathrm{sign}\rangle_{|w|}}. \tag{S6}$$

Here, we have used

$$\langle\ \square\ \rangle_{|w|} = \frac{\sum_{\mathrm{c}}\ \square\ |w(\mathrm{c})|}{\sum_{\mathrm{c}}|w(\mathrm{c})|}, \tag{S7}$$

to denote the expectation value obtained using $|w(\mathrm{c})|$ as the sampling probability. The sign problem introduces a cost that the average sign $\langle\mathrm{sign}\rangle_{|w|}$ tends to zero due to the frequent cancellation of positive and negative weights across different configurations, leading to the consequence that (S6) becomes a ratio between two tiny numbers. This is numerically unstable and introduces significant statistical errors. Specifically, it is proven that the error generally follows (9):

$$\Delta\langle O\rangle \propto \frac{1}{\langle\mathrm{sign}\rangle_{|w|}} \propto \mathrm{e}^{\tau N\Delta f}, \tag{S8}$$

where Δf denotes the difference in the free energy density between the actual fermionic system and its corresponding bosonic system. The exponential dependence of the error amplification factor on the imaginary time τ and the number of particles N means that QMC requires exponentially long computational times to achieve controllable statistical errors when solving ground-state problems of quantum systems in the thermodynamic limit.

In subsequent analyses, we use the average sign $\langle\mathrm{sign}\rangle_{|w|}$ to measure the severity of the sign problem. The lower value of the average sign $\langle\mathrm{sign}\rangle_{|w|}$ indicates a more severe sign problem.

D. Applicability and limitations of the nonequilibrium approach

The proposed nonequilibrium method offers an efficient pathway for exploring ground-state properties by circumventing the sign problem in our model and significantly lowering computational cost. This makes it highly effective for mapping the phase diagram and extracting critical properties of the quantum phase transition. However, it is important to emphasize that this is not a universal solution for all models plagued by the sign problem. Here, we discuss the applicability and limitations of our approach. The nonequilibrium approach is subject to two key limitations that constrain its applicability:

1. One cannot take the imaginary time arbitrarily short in order to ensure that the sign problem is mild for all models. If the evolution time is too short, the system retains too much memory of the initial state, and the scaling theory breaks down. For instance, this breakdown of scaling theory occurs when the characteristic length scale of the evolution, $\xi_l \propto \tau^{1/z}$, becomes comparable to the system's ultraviolet (UV) cutoff—in our case, the lattice spacing (set to unity). Under this condition, the behavior of observables is dominated by non-universal, high-energy physics, rendering the scaling analysis invalid.

2. This method is applicable to the continuous quantum phase transitions. This method is applicable for studying continuous quantum phase transitions. Our approach can be applied to determine the ground-state phase diagram and to identify and locate possible QCPs. If a QCP exists, our method can accurately determine the critical exponents based on the scaling theory of continuous transitions. On the other hand, if the calculation reveals that the transition does not exhibit scaling behavior, it implies a first-order transition, for which there is currently no well-established scaling analysis framework to use. In addition, our method is not applicable deep in the ordered phase, far away from the transition point.

We begin by elaborating on the first limitation, and provide a framework for understanding when the method is effective and when it fails. In general, fixing a system size L for discussion, the effectiveness of our method depends on three characteristic imaginary-time scales: (1) the minimum time $\tau_{\text{neq.}}$ at which the nonequilibrium scaling theory becomes valid; (2) the minimum time $\tau_{\text{eq.}}$ required for conventional PQMC to project onto the ground state; and (3) the maximum time τ_{sign} before the sign problem becomes too severe to obtain reliable results. Empirically, $\tau_{\text{eq.}}$ varies slightly between models but is usually around two to three times the linear system size L. The time $\tau_{\text{neq.}}$ required for short-time scaling to apply is typically one or two orders of magnitude smaller than $\tau_{\text{eq.}}$. In contrast, τ_{sign} can differ drastically from model to model and is the dominant factor that determines whether our approach will be effective. This leads to three possible scenarios:

1. $\tau_{\text{neq.}} < \tau_{\text{eq.}} < \tau_{\text{sign}}$: the sign problem is mild, and equilibrium methods already work well. Our nonequilibrium method only improves computational efficiency.

2. $\tau_{\text{neq.}} < \tau_{\text{sign}} < \tau_{\text{eq.}}$: equilibrium methods fail due to the sign problem, but the nonequilibrium method still works. This is the type of situation our work is focused on.

3. $\tau_{\text{sign}} < \tau_{\text{neq.}} < \tau_{\text{eq.}}$: the sign problem is too severe even at short times. In this case, the nonequilibrium method also fails.

Because the sign problem behaves differently across models, τ_{sign} varies accordingly. Based on this classification, we can view sign-problematic strongly correlated models as falling into three broad categories. The general argument that a QCP can be approached using sufficiently short imaginary-time simulations where the sign problem remains mild is valid only in models of type 1 and type 2. It does not hold in type 3 models, where the sign problem is already severe even at short times. Naturally, our method is not a fully general solution to the sign problem in all cases. What it does provide is a practical and effective approach for models of type 2, which were previously inaccessible due to severe sign problems in equilibrium simulations. With our method, such models become tractable.

Within the same model and parameter set, τ_{sign} also depends on the system size L. Typically, τ_{sign} decreases as L increases. This is because the average sign scales exponentially with both the particle number—which grows with system size ($N \propto L^d$)—and τ, as described by (S8) (9), although exceptions have been noted (52, 62). Taking this size dependence into account, we can sketch a regime diagram in the (L, τ) plane with the three regimes described above, as illustrated in Fig. S1. This diagram clearly demarcates the three previously described regimes and highlights a key advantage of the nonequilibrium method: it grants access to significantly larger system sizes than those achievable with conventional equilibrium QMC.

The above classification only provides general criteria for when the nonequilibrium method is effective, while the quantitative determination of the nonequilibrium scaling regime in practical applications is illustrated in detail with procedures and examples in Sec. S2 B.

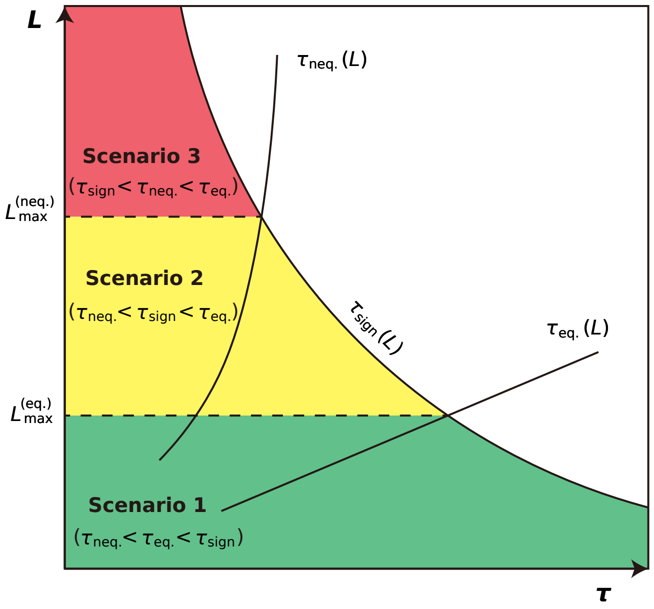

FIG. S1. Schematic illustration of the three scenarios regarding the sign problem. The shaded region indicates where the sign problem is not severe and simulations are feasible. The green region corresponds to scenario 1 ($\tau_{\text{neq.}} < \tau_{\text{eq.}} < \tau_{\text{sign}}$), where equilibrium methods also work. The yellow region corresponds to scenario 2 ($\tau_{\text{neq.}} < \tau_{\text{sign}} < \tau_{\text{eq.}}$), where only the nonequilibrium method is feasible. The red region corresponds to scenario 3 ($\tau_{\text{sign}} < \tau_{\text{neq.}} < \tau_{\text{eq.}}$), where even the nonequilibrium approach fails. The boundaries define the maximum accessible system sizes $L_{\max}^{(\text{eq.})}$ and $L_{\max}^{(\text{neq.})}$ for each method.

Next, we discuss another boundary case of this nonequilibrium short-time method, i.e., the first-order phase transition. In the main text, we have already demonstrated that our nonequilibrium method can determine the existence of a continuous phase transition based on scaling forms. The key criteria are: 1) For a given τL^{-z}, the crossing points of the correlation-length ratio or Binder ratio curves converge to a single point as the system size increases (dimensionless quantities exhibit scale invariance at the critical point). 2) The nonequilibrium critical relaxation processes of physical quantities such as the structure factor and fermion correlation display scaling collapse.

In fact, we are also able to identify a first-order phase transition during the short-time evolution through opposite characteristics: 1) The crossing points of the correlation-length ratio or Binder ratio curves do not converge to a single point. 2) The nonequilibrium critical relaxation processes of physical quantities such as the structure factor and fermion correlation cannot be well scaled to collapse. Additionally, 3) due to the coexistence of two phases at a first-order phase transition, the Binder ratio typically shows negative dips at the transition point, and the Monte Carlo sampling distribution of the structure factor exhibits a double peak. The emergence of negative dips in the results of Binder ratio is a hallmark of the first-order transition.

As a typical example, we demonstrate how to identify the first-order phase transition in the $q = 6$ quantum Potts chain during short imaginary time evolution. The Hamiltonian is given by:

$$H = -qJ \sum_i \sum_{m=0}^{q-1} P_i^{(m)} P_{i+1}^{(m)} - h \sum_i \sum_{m \neq n} |m\rangle_i \langle n| \,, \tag{S9}$$

where $P_i^{(m)} \equiv |m\rangle_i \langle m|$ is the projection operator on site i, and the tuning parameter is $g \equiv h/J$. For $g < 1$, the ground state is in the ferromagnetic phase, and for $g > 1$, it is in the paramagnetic phase. For the case of $q = 6$, a first-order phase transition occurs at $g_c = 1$. We use the time-evolving block decimation (TEBD) method to simulate the system's imaginary time evolution starting from an ordered ferromagnetic initial state (e.g., all sites choosed into $m = 0$ state) and observe the order parameter M and Binder ratio R:

$$M \equiv \frac{1}{L} \sum_{i=1}^{L} s_i \,, \qquad R \equiv 1 - \frac{\langle M^4 \rangle}{3 \langle M^2 \rangle^2} \,, \tag{S10}$$

where $s_i \equiv \frac{q}{q-1} \left(P_i^{(0)} - \frac{1}{q} \right)$. Using the same procedure as in the main text, we take a short imaginary time $\tau/L = 0.3$. The variation of Binder ratio R with g is shown in Fig. S2a. The curves for different system sizes do not intersect at

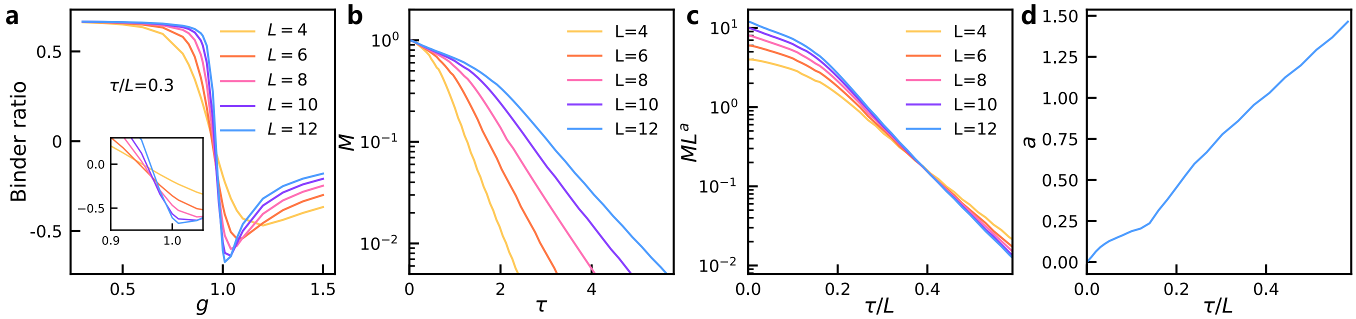

FIG. S2. **First-order phase transition characteristics in the $q = 6$ quantum Potts chain observed during short imaginary time evolution.** **a**, Binder ratio versus g for different system sizes, where the curves do not intersect at a single point, and negative dips are observed. The emergence of negative dips in the Binder ratios is a hallmark of first-order transition. **b**, Imaginary time relaxation of the order parameter M starting from the ordered phase at $g = 1$. **c**, Failure of scaling collapse for **b**, with $a = 1.0$ as an example. **d**, Fitting $M \propto L^{-a}$ for fixed τ/L, where the value of a does not converge as τ/L increases.

a single point, and there are distinct negative dips, which are characteristic of a first-order phase transition and can appear with short imaginary time evolution at $\tau/L = 0.3$. Fig. S2b shows the imaginary time relaxation of the order parameter M starting from the ordered phase at $g = 1$, which decays exponentially with τ. Fig. S2c demonstrates the failure of scaling collapse for M, using a scaling exponent $a = 1.0$ as an example. Adjusting a does not allow these curves to collapse or partially collapse. If we fix τ/L and perform scaling fitting according to the form $M \propto L^{-a}$, the results for a are shown in Fig. S2d, and they do not converge as τ/L increases. These results, which violate scaling forms, clearly exclude the possibility of a continuous phase transition here. This example illustrates that a first-order phase transition can be distinguished from a continuous phase transition even during short imaginary time evolution. However, for such cases, although the rough phase diagram can still be determined, the precise location of the transition point may not be accurately obtained within the short imaginary-time regime since the current scaling form no longer holds, and may instead require extrapolation from finite-time data.

E. Guiding principles for choosing the value of τ/L^z in simulations

In the main text, we adopt the form $\tau = (\text{const.}) \times L^z$ to identify quantum critical points. We use coefficients 0.3 in Figs. 1b–1c and 2a–2b, and 0.25 in Figs. 3b–3c. When choosing these specific coefficients, we carefully balanced three considerations: the severity of the sign problem, the validity of the scaling theory, and the numerical precision of the estimated critical point. In general, the following guiding principles apply:

1. The severity of the sign problem is the most important factor. Usually, slightly increasing the value of τ/L^z makes the sign problem significantly worse, and vice versa. For example, if the coefficient is increased from 0.3 to 0.6, the sign problem becomes notably more severe, significantly reducing the accessible system size. From this guiding principle, τ/L^z should be chosen as small as possible.

2. Another important factor is the validity of the scaling theory. If τ/L^z is too small, the nonequilibrium scaling theory may not hold well at currently accessible finite sizes. Specifically, for example, when it is taken below 0.1, from Figs. 1d, 2c, and 3d one can see that the data collapse gradually starts to break down, meaning finite-size effects become significant. This condition is relatively flexible. As long as τ/L^z is above a certain threshold, the scaling holds well, and variations in the coefficient do not significantly affect the results. Values such as 0.25, 0.3, and 0.5 are typically used in the literature (50, 78), where estimates of critical points at different τ/L^z values were found to agree within statistical error, providing a useful self-consistency check.

3. Another somewhat subtle factor is the resolution of the critical point. Even within the valid scaling regime, choosing a smaller τ/L^z broadens the nonequilibrium critical region. This broadening manifests as a diminished dependence of the dimensionless correlation length ratio R on system size L over a wide range of the tuning parameter U near U_c, making the crossing point of R curves (such as in Fig. 1b) less sharp. This leads to reduced numerical precision in locating the critical point. Therefore, from this perspective, it is preferable to choose a somewhat larger τ/L^z to enhance resolution.

In summary, when applying the nonequilibrium approach to determine quantum critical points, one must balance these considerations within the valid scaling regime. The goal is to choose a value of τ/L^z that optimizes both precision and accuracy. In our experience, the severity of the sign problem is often the most decisive factor.

S2. MORE DETAILS FOR THE SINGLE-DIRAC-FERMION HUBBARD MODEL

A. Sign problem behaviors

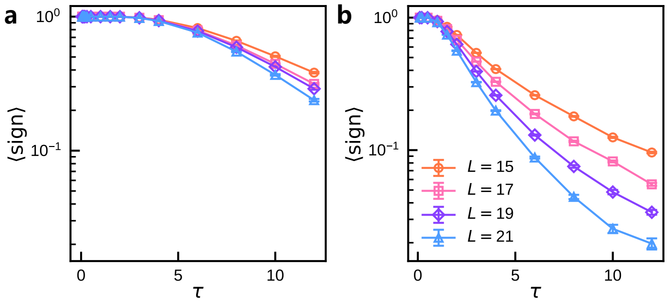

FIG. S3. **Evolution of the average sign at the critical point.** **a**, Evolution from the DSM initial state. **b**, Evolution from the FM initial state.

Fig. S3 shows that near the critical point of the single-Dirac-fermion Hubbard model, the average sign $\langle \mathrm{sign} \rangle$ decays in the imaginary-time relaxation with the Dirac semimetal (DSM) and the ferromagnetic (FM) initial states. We find that different initial states can have different decay rates. In the relaxation with the DSM initial state, the average sign decays more slowly. The data presented in Fig. 1 of the main text show the relaxation results starting from the DSM initial state.

B. Verification of the QCP and critical exponents

Several physical quantities are needed to describe the universal scaling behaviors near the QCP. The spin structure factor $S(\boldsymbol{k})$ with momentum $\boldsymbol{k}$ is defined as

$$S(\boldsymbol{k}) \equiv \frac{1}{L^{2d}} \sum_{i,j} \mathrm{e}^{\mathrm{i}\boldsymbol{k}\cdot(\boldsymbol{r}_i - \boldsymbol{r}_j)} \langle S_i^z S_j^z \rangle, \tag{S11}$$

where the local spin operator is $S_i^z \equiv \boldsymbol{c}_i^\dagger \sigma^z \boldsymbol{c}_i$ with $\boldsymbol{c}^\dagger \equiv (c_\uparrow^\dagger, c_\downarrow^\dagger)$. In addition, the correlation length ratio R_{FM} is defined as

$$R_{\mathrm{FM}} \equiv 1 - \frac{S(\boldsymbol{k} = \Delta\boldsymbol{k})}{S(\boldsymbol{k} = 0)}, \tag{S12}$$

where $\Delta\boldsymbol{k} = \frac{1}{L}\boldsymbol{b_1} + \frac{1}{L}\boldsymbol{b_2}$ is the minimum momentum of electrons in a lattice with periodic boundary conditions, and $\boldsymbol{b_1}, \boldsymbol{b_2}$ are the reciprocal lattice vectors.

The fermion correlation function $G_{\mathrm{f}}(\boldsymbol{k})$ is defined as

$$G_{\mathrm{f}}(\boldsymbol{k}) \equiv \frac{1}{L^2} \sum_{ij} \mathrm{e}^{\mathrm{i}\boldsymbol{k}(\boldsymbol{r}_i - \boldsymbol{r}_j)} \langle c_{i\uparrow}^\dagger c_{j\downarrow} \rangle \, . \tag{S13}$$

We remark that the fermionic correlation $G_{\mathrm{f}}(\boldsymbol{k})$ is defined in momentum space, as commonly done in related works (50, 55, 57, 79, 80). Compared to real-space correlations, which often decay in an oscillatory manner and thus exhibit somewhat subtle finite-size effects (e.g., as it may depend on the even-odd parity of the distance or the size), momentum-space correlations are often more straightforward and robust for analysis. Physically, the momentum-space fermionic correlation defined in Eqs. (S13), (S22) and (S34) captures the quasiparticle weight Z, which characterizes the discontinuity in the occupation number across the Fermi surface. Specifically, $Z = \lim_{L\to\infty} 2\,|G_{s\bar{s}}(\Delta\boldsymbol{k})|$, where s and $\bar{s}$ denote the two components of the Dirac spinor, corresponding to spin $(\uparrow, \downarrow)$ or sublattice (A, B) degrees of freedom in different models. In contrast, momentum-space correlations between the same spinor components are trivial,

$G_{ss}(k) = 1/2$ for all k, due to spontaneous breaking of chiral symmetry. For detailed derivations and discussions, see Refs. (50, 79).

In the main text and figures of data, we abbreviate $S_{\mathrm{FM}} \equiv S(\boldsymbol{k} = \mathbf{0})$ and $G_{\mathrm{f}} \equiv G_{\mathrm{f}}(\boldsymbol{k} = \Delta\boldsymbol{k})$, unless otherwise specified.

The correlation length ratio R_{FM} is a dimensionless quantity. In the nonequilibrium critical region, the correlation length ratio R_{FM} satisfies the following scaling form:

$$R_{\mathrm{FM}}(g, \tau, L) = f_R(gL^{1/\nu}, \tau L^{-z}), \tag{S14}$$

where $g = U - U_c$. To determine the quantum critical point U_c, we fix τL^{-z} to be constant (e.g., we take $\tau L^{-z} = 0.3$ in the main text), so the scaling form of R_{FM} reduces to $R(g, \tau, L) = f_{R1}(gL^{1/\nu})$, which is similar to the traditional finite-size scaling. Accordingly, the critical point can be determined by the intersection of curves of R_{FM} versus U for different L. We fit U_c and ν based on the expansion of the scaling form:

$$R_{\mathrm{FM}}(g, L) = f_{R1}(gL^{1/\nu}) = \sum_{n=0}^{n_{\max}} a_n g^n L^{n/\nu}. \tag{S15}$$

where we appropriately truncate the scaling functions with polynomials (57).

In the main text, based on the results from the DSM initial state, we fit according to Eq. (S15) and obtain $U_c = 7.220(37), 1/\nu = 1.18(3)$ at $\tau = 0.3L^z$. Here we supplement data in Figs. S4c-S4d, where τ is extended to $0.5L^z$, giving $U_c = 7.225(34), 1/\nu = 1.16(9)$ at $\tau = 0.5L^z$, which is consistent with the results at $\tau = 0.3L^z$ within error bars. This demonstrates that the imaginary time we used has already entered the nonequilibrium scaling regime and that the critical point values have converged. On the other hand, we have also considered the FM initial state, as shown in Figs. S4a-S4b, which gives $U_c = 7.214(44), 1/\nu = 1.05(10)$ at $\tau = 0.5L^z$, also close to the results obtained from the DSM initial state. These results not only confirm the values of the critical point U_c and the critical exponent $1/\nu$, but also show that the initial states can be chosen flexibly in our method, which provides a route to achieve reliable values of critical exponents by benchmarking the results with different initial states. This flexibility offers more possible options for alleviating the sign problem.

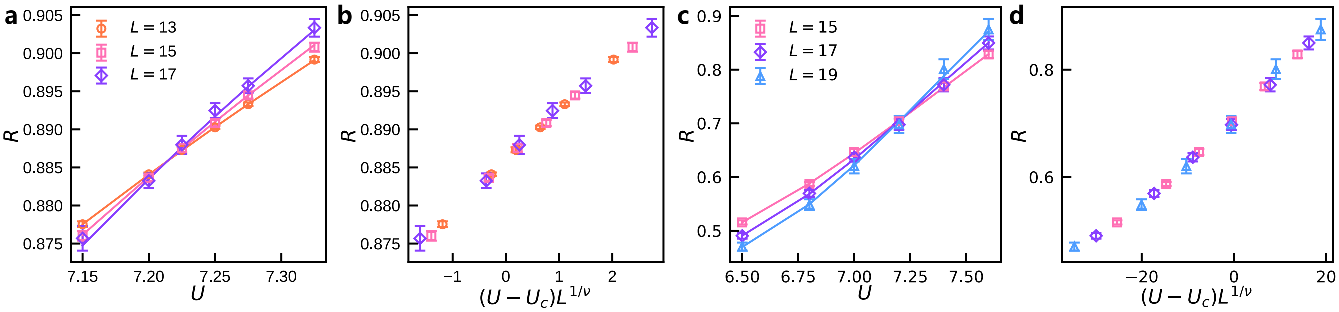

FIG. S4. **Verification of quantum criticality using different initial states and imaginary times.** **a**–**b**, With the FM initial state and $\tau = 0.5L^z$, the data collapse yields $U_c = 7.214(44)$ and $\nu^{-1} = 1.05(10)$. **c**–**d**, With the DSM initial state and $\tau = 0.5L^z$, the data collapse yields $U_c = 7.225(34)$ and $\nu^{-1} = 1.16(9)$.

The comparison of results from different initial states, as shown in Table S1, provides an excellent bootstrap-style self-consistency check for the accuracy of our method, which we further illustrate below through the determination of the anomalous dimensions.

The anomalous dimensions of the bosonic field η_ϕ and the fermionic field η_ψ can be determined by the following scaling relations:

$$S(\boldsymbol{k} = \mathbf{0}) = L^{-(1+\eta_\phi)} f_S\left(gL^{1/\nu}, \tau L^{-z}\right), \tag{S16}$$

$$G_{\mathrm{f}}(\boldsymbol{k} = \Delta\boldsymbol{k}) = L^{-\eta_\psi} f_G\left(gL^{1/\nu}, \tau L^{-z}\right). \tag{S17}$$

We obtain $\eta_\phi = 0.34(5)$ and $\eta_\psi = 0.131(20)$ from the data collapse in the relaxation dynamics at $g = 0$, as shown in Fig. S5. Note that only the data within the nonequilibrium scaling region are included in the data collapse analysis. Below we present the general principles and technical details for extracting the critical exponents.

TABLE S1. **Comparison of critical properties for the single-Dirac-fermion Hubbard model calculated by different methods.** The method used in this work is the nonequilibrium short-time PQMC.

Methods	$\boldsymbol{U_c}$	$\boldsymbol{\nu^{-1}}$	$\boldsymbol{\eta_\phi}$	$\boldsymbol{\eta_\psi}$
This work (from DSM, $\tau = 0.3L^z$)	7.220(37)	1.18(3)	0.36(3)	0.134(3)
This work (from DSM, $\tau = 0.5L^z$)	7.225(34)	1.16(9)	-	-
This work (from FM, $\tau = 0.5L^z$)	7.214(44)	1.05(10)	0.35(3)	0.136(14)
Gutzwiller-PQMC (equilibrium) (55)	7.275(25)	1.19(3)	0.31(1)	0.136(5)
FRG (58)	-	1.229	0.372	0.131

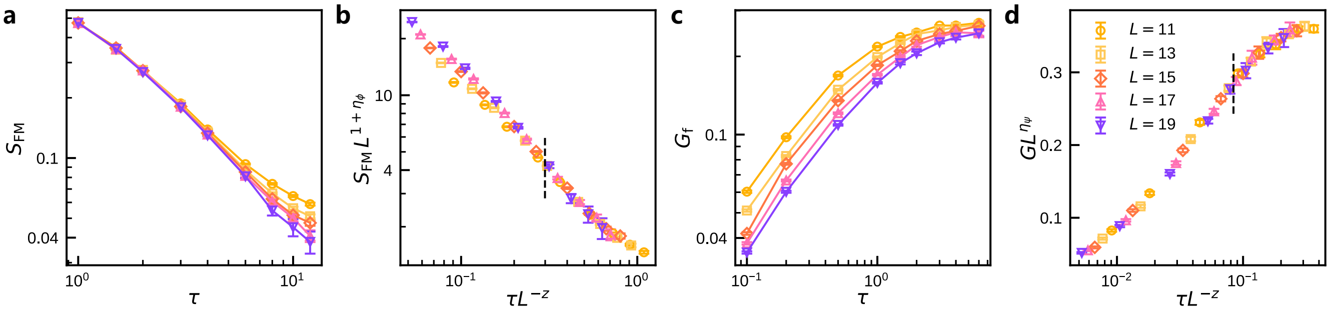

FIG. S5. **Relaxation dynamics at QCP with FM initial state in single-Dirac-fermion Hubbard model. a-b**, Curves of $S_{\rm FM} \equiv S(\boldsymbol{k} = \boldsymbol{0})$ versus τ for different sizes before and after rescaling. **c-d**, Curves of $G_{\rm f} \equiv G_{\rm f}(\boldsymbol{k} = \Delta\boldsymbol{k})$ versus τ before and after rescaling. Data collapse in the relaxation dynamics shows $\eta_\phi = 0.34(5)$ and $\eta_\psi = 0.131(20)$. Only the interval with sufficiently large τL^{-z} is used for the data collapse, with the technical details shown in Fig. S6.

As we stated in Sec. S1 E, when τL^{-z} is sufficiently large, the system enters the nonequilibrium scaling region, and the critical exponents can be accurately extracted during the nonequilibrium process without dependence on the initial state. In contrast, for too small values of τL^{-z}, the system remains too close to the initial state and lies outside the nonequilibrium scaling region governed by the critical point, where the scaling relations no longer hold. In practice, we apply this criterion to precisely determine the critical exponents and delineate the non-equilibrium scaling region. During data collapse analysis, we systematically vary the lower bound of τL^{-z} , denoted as $(\tau L^{-z})_{\rm min}$, and examine how the fitted critical exponents vary with $(\tau L^{-z})_{\rm min}$, as shown in Figs. S6a and e. As $(\tau L^{-z})_{\rm min}$ for the data collapse increases, the fitted critical exponents gradually converge and, within the resolution of the error bars, no longer change with $(\tau L^{-z})_{\rm min}$. Moreover, the critical exponents obtained from nonequilibrium processes starting from different initial states converge to the same results within the error bars—this is the hallmark of having entered the nonequilibrium scaling region.

Regarding the critical exponent η_ϕ in the single-Dirac-fermion Hubbard model, Fig. S6a shows that η_ϕ converges once $(\tau L^{-z})_{\rm min} > 0.25$, and the results obtained from nonequilibrium processes starting from different initial states are consistent. We use the reduced χ^2_ν to assess the quality of the data collapse:

$$\chi^2_\nu = \frac{1}{\nu} \sum_{i=1}^{N} \sum_{L}^{N_L} \frac{(y_{iL} - \mu_i)^2}{\Delta y_{iL}^2} \,. \tag{S18}$$

For the rescaled curves corresponding to different system sizes L (N_L curves in total), we perform linear interpolation and then uniformly sample $N = 50$ values of τL^{-z} to obtain the curve ordinates y_{iL} and their uncertainties Δy_{iL}. We then compute the weighted mean $\mu_i = \sum_L w_{iL}\, y_{iL} / \sum_L w_{iL}$ with weights $w_{iL} = 1/\Delta y_{iL}^2$. The degrees of freedom for the reduced chi-square are $\nu = N(N_L - 1)$. As shown in Fig. S6b, when $(\tau L^{-z})_{\rm min}$ is very small, $\chi^2_\nu \gg 1$, indicating very poor collapse quality and that the scaling form cannot describe such short $(\tau L^{-z})_{\rm min}$. As $(\tau L^{-z})_{\rm min}$ increases, χ^2_ν decreases. Around $0.2 < (\tau L^{-z})_{\rm min} < 0.35$, χ^2_ν approaches 1, where the quality of the data collapse is optimal. Further increasing $(\tau L^{-z})_{\rm min}$ leads to $\chi^2_\nu < 1$, which implies overfitting. This occurs because data points at larger τL^{-z} suffer from more severe sign problems and thus have larger errors, exceeding the resolution of the collapse. Taking into account the convergence behavior in Fig. S6a, the consistency between results from different initial states, and the collapse quality shown in Fig. S6b, we finally choose $(\tau L^{-z})_{\rm min} = 0.3$ as the lower bound for τL^{-z} in the data collapse analysis of the structure factor S for the single-Dirac-fermion Hubbard model. We evaluate the uncertainty of the critical exponent using a resampling technique. As shown in Fig. S6c, we randomly perturb the data of the

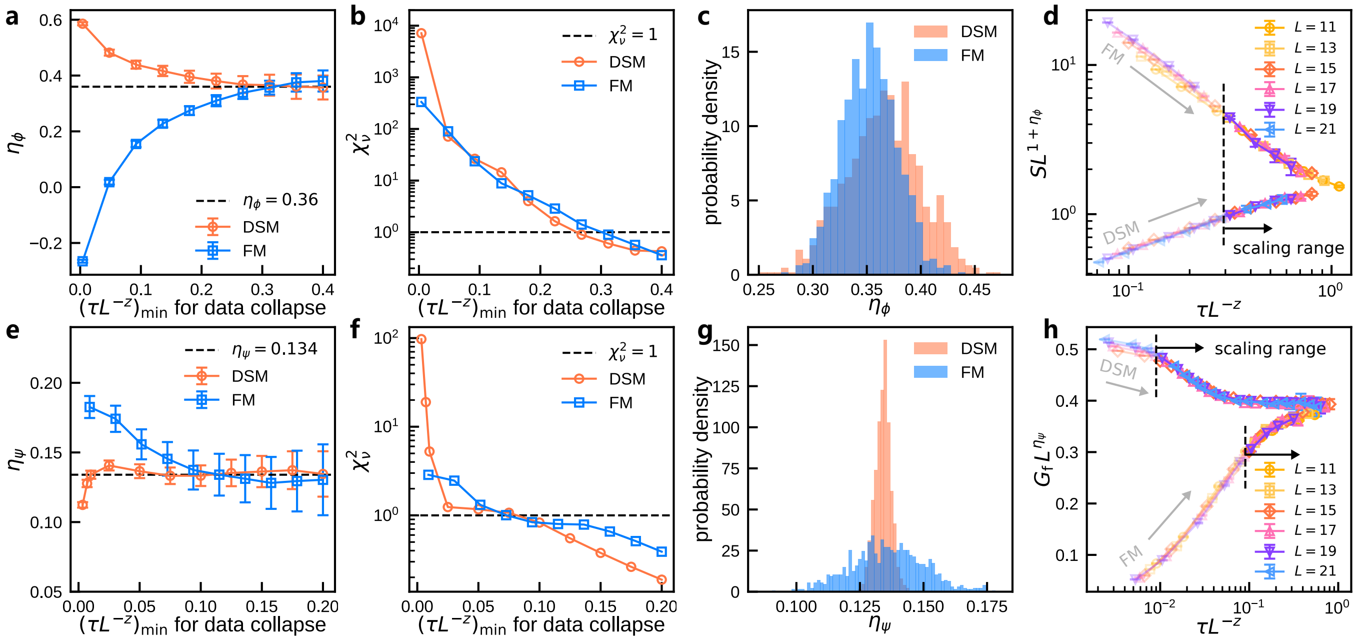

FIG. S6. **Technical details of determining the critical exponents in the single-Dirac-fermion Hubbard model via data collapse. a**–**d**, Determination of the critical exponent η_ϕ. **a**, Fitted values of η_ϕ versus the lower bound $\left(\tau L^{-z}\right)_{\min}$ used in the data collapse analysis. The legend "DSM" denotes data collapse performed with the Dirac semi-metal initial state (the lower set of curves in **d**); the legend "FM" denotes data collapse performed with the ferromagnetic initial state (the upper set of curves in **d**). **b**, Reduced χ^2_ν of the data collapse versus $\left(\tau L^{-z}\right)_{\min}$. **c**, Distribution of the fitted η_ϕ obtained from 1000 resamplings with $\left(\tau L^{-z}\right)_{\min} = 0.3$. The results are $\eta_\phi = 0.36(3)$ with the DSM initial state and $\eta_\phi = 0.35(3)$ with the FM initial state. **d**, Scaling collapse of curves of the structure factor S_{FM} versus rescaled τ at U_c. **e**–**h**, Determination of the critical exponent η_ψ. **e**, Fitted values of η_ψ versus $\left(\tau L^{-z}\right)_{\min}$. The legend "DSM" denotes data collapse performed with the DSM initial state (the upper set of curves in **h**); the legend "FM" denotes data collapse performed with the FM initial state (the lower set of curves in **h**). **f**, Reduced χ^2_ν of the data collapse versus $\left(\tau L^{-z}\right)_{\min}$. **g**, Distribution of the fitted η_ψ obtained from 1000 resamplings with $\left(\tau L^{-z}\right)_{\min} = 0.01$ for the DSM initial state and $\left(\tau L^{-z}\right)_{\min} = 0.1$ for the FM initial state. The results are $\eta_\psi = 0.134(3)$ for the DSM initial state and $\eta_\psi = 0.136(14)$ for the FM initial state. **h**, Scaling collapse of curves of the fermion correlation G_{f} versus rescaled τ at U_c.

structure factor S according to the size of the error bars of the original data and then perform the data collapse analysis again to extract η_ϕ. Figure S6c presents the histogram of η_ϕ obtained from 1000 resamplings, showing consistent results between the DSM and FM initial states. By fitting the histogram with a Gaussian distribution, we obtain the critical exponent as $\eta_\phi = 0.36(3)$ for the DSM initial state and $\eta_\phi = 0.35(3)$ for the FM initial state. Figure S6d displays the rescaled data collapse using these results. The black dashed line marks $\tau L^{-z} = 0.3$, with the region to the right included in the scaling analysis, where curves of different system sizes collapse perfectly. The region to the left of the dashed line is outside the scaling regime, and the deviations from scaling can be seen from the degree of non-overlap between curves. Figure S6d also shows that the system has not yet evolved to equilibrium (which typically requires $\tau L^{-z} \sim 2$–3). Nevertheless, we are able to determine the accurate ground-state critical exponents from nonequilibrium data. Comparing Figs. S6a and S6d, for the system sizes we studied, the τL^{-z} needed for the convergence of η_ϕ is about one order of magnitude smaller than that required for the convergence of the structure factor S. At larger system sizes, the nonequilibrium critical region will be even broader.

The same applies to other similar data collapse figures: our data collapse analysis is *only* performed using data within the defined scaling range, which appears after a microscopic nonuniversal time scale. Data points at very small τL^{-z} lie outside this range and are, therefore, excluded from the analysis. However, it should be emphasized that the this is not the specific issue for the short-time scaling. Even for the more popular finite-size scaling, when the lattice size is too small to enter the scaling region, the finite-size scaling can lose its efficacy. The boundary of this scaling range is critical for the practical application of our method, as it dictates the minimum permissible τL^{-z} and thus the extent to which the sign problem can be alleviated. For this reason, we deliberately presented the crossover from scaling violation to scaling satisfaction in these figures. This approach provides a direct visualization of the scaling-range boundary, elucidating our rationale for selecting appropriate τL^{-z} values and preventing the misconception that τL^{-z} can be chosen arbitrarily small. We explicitly mark the scaling range in these figures with dash lines.

From the above analysis procedure, it is clear that determining critical points and critical exponents using nonequilibrium scaling is highly controllable in terms of accuracy. We can assess the accuracy not only by examining the asymptotic convergence and the quality of the data collapse, but more importantly, by the fact that nonequilibrium evolutions from different initial states are governed by the same ground-state critical exponents. The consistency of the critical points and critical exponents obtained with different initial states is smoking gun evidence that our results are sufficiently accurate and self-consistent. This is a significant advantage of the nonequilibrium approach compared with finite-temperature scaling or finite-size scaling in the conventional equilibrium approaches. Even in situations where the sign problem is particularly severe and prevents accurate results within the scaling range, the early-time results from different initial states can still bracket a controlled range for the critical points and critical exponent.

Table S1 compares the results in the present work with those of other methods. The consistent results shown in this table demonstrate that the method based on the short-time dynamics can accurately determine the critical properties of the ground-state QCP with much fewer computational costs.

C. Procedure for determining the dynamical exponent z

The quantum phase transitions studied in this work fall into the Dirac QCP universality class, for which the dynamical exponent is known to be $z = 1$. However, applying this method to systems with an unknown dynamical exponent requires a self-consistent treatment, as both z and the critical point should be determined together. To address this, we introduce a general procedure for extracting z without prior knowledge of the critical point. We then demonstrate the efficacy of this procedure by applying it to the single-Dirac-fermion Hubbard model, providing a detailed analysis of the numerical results.

We introduce a new dimensionless ratio:

$$R_0(U,\tau) \equiv \frac{S_{\mathrm{FM}}(U,2\tau)}{S_{\mathrm{FM}}(U,\tau)}, \tag{S19}$$

where S_{FM} is the zero-momentum structure factor. Suppose we do not know the precise values of U_c and z initially; we determine them via the following iterative steps:

Step 1. We first select a relatively large system size L, for instance, $L = 23$ in Fig. S7a, such that the factor τL^{-z} has negligible influence on the scaling of R_0. According to the scaling form $R_0 = 2^{\frac{1+\eta_\phi}{z}} f_{R_0}(g\tau^{\frac{1}{\nu z}})$, the crossing point of R_0 curves for different τ provides an initial estimate of the critical point, $U_c = 6.92(1)$, as shown in Fig. S7a. Note that this estimate of U_c may not yet be highly accurate, since the finite-size effects involving τL^{-z} have only been approximately neglected.

Step 2. At the tentative critical point $U = 6.92$ obtained from Step 1, we estimate the dynamical exponent z from the scaling form of the correlation length ratio, $R_{\mathrm{FM}} = f_R(\tau L^{-z})$. In Fig. S7b-S7c, by performing data collapse of the relaxation dynamics of R_{FM}, we obtain an initial estimate for the dynamical exponent: $z = 1.68(7)$. Again, this initial estimate may still have uncertainties.

Step 3. Next, we fix the value of τL^{-z} using the estimate $z = 1.68$ from Step 2 and refine the critical point determination using the nonequilibrium method described in the main text. As shown in Fig. S7d, we obtain an improved estimate of the critical point, $U_c = 7.19(1)$.

Further iterations. Returning to Step 2, we re-estimate z at the updated critical point $U = 7.19$. As shown in Fig. S7e-S7f, this yields an improved value $z = 1.21(14)$. One can further iterate Steps 2 and 3 to progressively enhance the accuracy of both U_c and z.

By repeatedly iterating Steps 2 and 3, the estimates for both U_c and z converge towards stable values. In Fig. S7, after three rounds of iterations, we obtain final estimates of $U_c = 7.23(1)$ and $z = 1.07(9)$, which are consistent within error bars with the result $U_c = 7.220(37)$ presented in the main text and the known Dirac QCP value of $z = 1$.

This procedure can also be generally applied to other models and different types of QCP, even when both the location of the critical point and the value of z are initially unknown.

S3. MORE DETAILS FOR THE SPINLESS t-V MODEL

A. Sign problem behaviors

As shown in Fig. S8, for both DSM initial state and CDW initial state, the average sign in the short-time stage is close to one, indicating the sign problem is very weak. In particular, for $\tau = 0.3L^z$, as shown in the insets of Fig. S8,

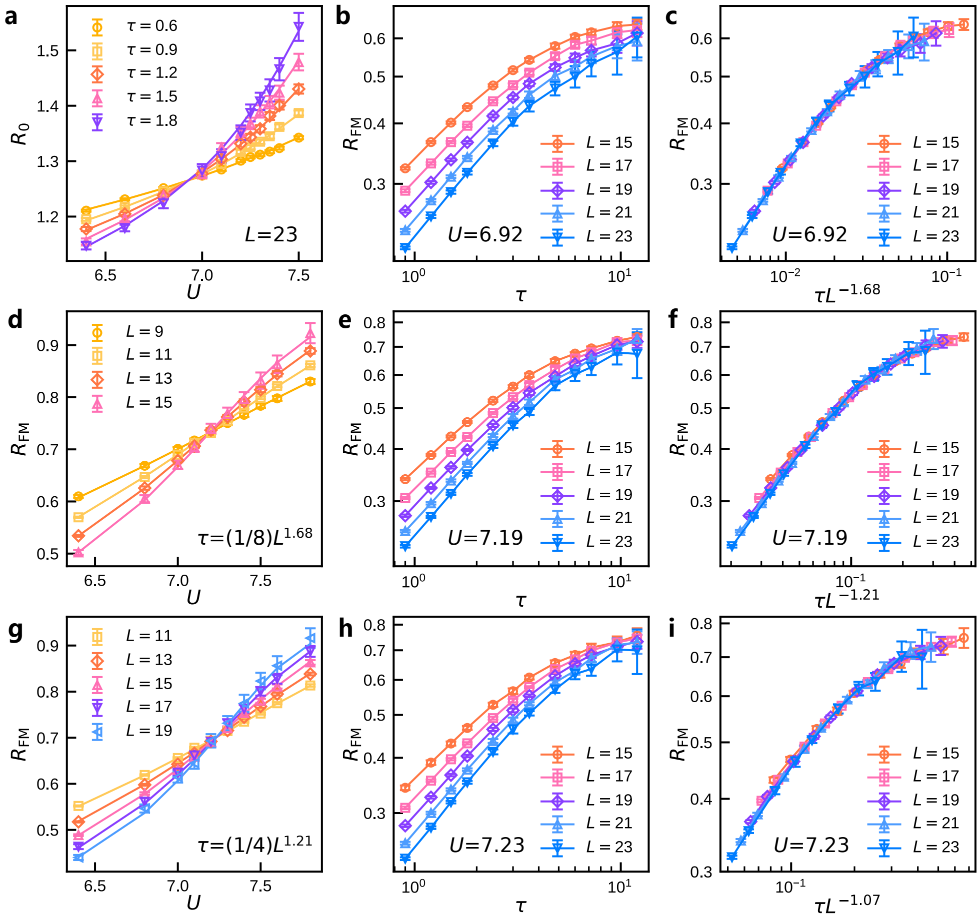

FIG. S7. **Determining the critical point U_c and the dynamical exponent z for the single-Dirac-fermion Hubbard model.** **a**, Curves of dimensionless ratio $R_0(U,\tau) \equiv S_{\mathrm{FM}}(U,2\tau)/S_{\mathrm{FM}}(U,\tau)$ versus U at different τ. The crossing point gives an initial estimate of the critical point $U_c = 6.92(1)$. **b**, Relaxation dynamics of the correlation length ratio R_{FM} at $U = 6.92$. **c**, Data collapse of **b** yields an initial estimate of the dynamical exponent $z = 1.68(7)$. **d**, By fixing $\tau = \frac{1}{8}L^{1.68}$, the crossing point of R_{FM} versus U curves gives an improved estimate of the critical point $U_c = 7.19(1)$. **e**, Relaxation dynamics of the correlation length ratio R_{FM} at $U = 7.19$. **f**, Data collapse of **e** yields an improved estimate of the dynamical exponent $z = 1.21(14)$. **g**, By fixing $\tau = \frac{1}{4}L^{1.21}$, the crossing point of R_{FM} versus U curves gives an improved estimate of the critical point $U_c = 7.23(1)$. **h**, Relaxation dynamics of the correlation length ratio R_{FM} at $U = 7.23$. **i**, Data collapse of **e** yields an improved estimate of the dynamical exponent $z = 1.07(9)$.

the system almost remains sign-free near the critical point $V_c = 1.35(1)$ determined in the main text.

Incidentally, Fig. S8 shows that the decay rate of $\langle \mathrm{sign} \rangle$ does not monotonically change with the system size L. In some cases, a larger system size L results in a weaker sign problem. Such phenomena have also been reported in the equilibrium projector QMC study (62) and finite-temperature DQMC (52).

B. Verification of the QCP and critical exponents

For this model, the ordered phase is the charge density wave (CDW) state, for which the structure factor S_{CDW} can be defined as:

$$S_{\mathrm{CDW}}(\boldsymbol{k}) \equiv \frac{1}{L^{2d}} \sum_{i,j} \mathrm{e}^{\mathrm{i}\boldsymbol{k}\cdot(\boldsymbol{r}_i - \boldsymbol{r}_j)} \langle m_i m_j \rangle, \tag{S20}$$

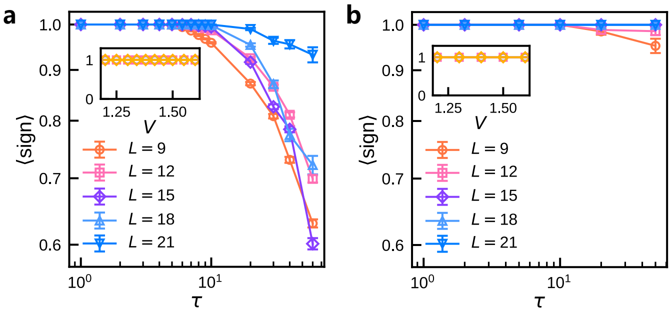

FIG. S8. **Evolution of average sign at the QCP (inset shows $\langle\text{sign}\rangle$ versus V near the QCP for $\tau = 0.3L^z$). a**, Evolution from the DSM initial state. **b**, Evolution from the CDW initial state.

where the local order operator is $m_i \equiv \frac{1}{2}(n_{i,A} - n_{i,B})$, which represents the difference in particle number density between the two sublattices in a unit cell. The associated correlation length ratio R_{CDW} is defined as:

$$R_{\text{CDW}} \equiv 1 - \frac{S_{\text{CDW}}(\boldsymbol{k} = \Delta\boldsymbol{k})}{S_{\text{CDW}}(\boldsymbol{k} = 0)}. \tag{S21}$$

The fermion correlation $G_{\text{f}}(\boldsymbol{k})$ is defined similarly to Eq. (S13):

$$G_{\text{f}}(\boldsymbol{k}) \equiv \frac{1}{L^2} \sum_{ij} \mathrm{e}^{\mathrm{i}\boldsymbol{k}(\boldsymbol{r}_i - \boldsymbol{r}_j)} \left\langle c_{i,A}^{\dagger} c_{j,B} \right\rangle . \tag{S22}$$

Here, the sublattice indices A and B function as Dirac spinor indices. In the main text and figures of data, we abbreviate $S_{\text{CDW}} \equiv S_{\text{CDW}}(\boldsymbol{k} = \boldsymbol{0})$ and $G_{\text{f}} \equiv G_{\text{f}}(\boldsymbol{k} = \text{K} + \Delta\boldsymbol{k})$, where $\text{K} = \left(\pm\frac{4\pi}{3}, 0\right)$ represents the momentum at the Dirac points.

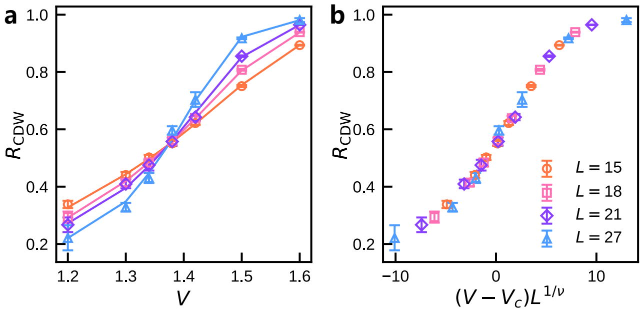

FIG. S9. **Determination of the critical point and $1/\nu$ with DSM initial state. a**, At $\tau = 0.3L^z$, curves of R_{CDW} versus V for different sizes intersect at $V_c = 1.37(2)$. **b**, Data collapse of curves of R_{CDW} versus rescaled $(V - V_c)$ with $\nu = 0.79(5)$.

In Fig. 2 of the main text, we showed the results of determination of critical properties via the short-time dynamics from the ordered CDW initial state. In contrast, here we show consistent results can also be obtained from the DSM initial state.

Fig. S9 illustrates the correlation length ratio R_{CDW} as a function of interaction strength V at $\tau = 0.3L^z$. We fit the data in Fig. S9a using the scaling form in Eq. S15, determining the intersection point of the curves for different sizes as $V_c = 1.37(2)$ and the scaling collapse exponent as $\nu = 0.79(5)$. These results are close to those obtained by equilibrium methods (59, 60) and the short-time dynamics with ordered CDW initial state discussed in the main text. Fig. S10 shows the relaxation dynamics of $S_{\text{CDW}} = S_{\text{CDW}}(\boldsymbol{k} = 0)$ and $G_{\text{f}} = G_{\text{f}}(\boldsymbol{k} = \text{K} + \Delta\boldsymbol{k})$ starting from the DSM initial state. Their scaling behavior is described by Eq. (S16) and Eq. (S17). According to the scaling collapse of the evolution of S_{CDW} in Fig. S10a-S10b, one finds $\eta_\phi = 0.44(2)$. In addition, from the scaling collapse of the evolution of G_{f} in Fig. S10c-S10d, we obtain $\eta_\psi = 0.072(4)$. The value of η_ϕ is close to that obtained by the equilibrium methods (59, 60) and the short-time dynamics with ordered CDW initial state discussed in the main text; while the value of η_ψ is close to the FRG result (58), and also consistent with that obtained from the CDW initial state shown in the main text. Consequently, the results of critical properties in the t-V model further demonstrate the efficiency

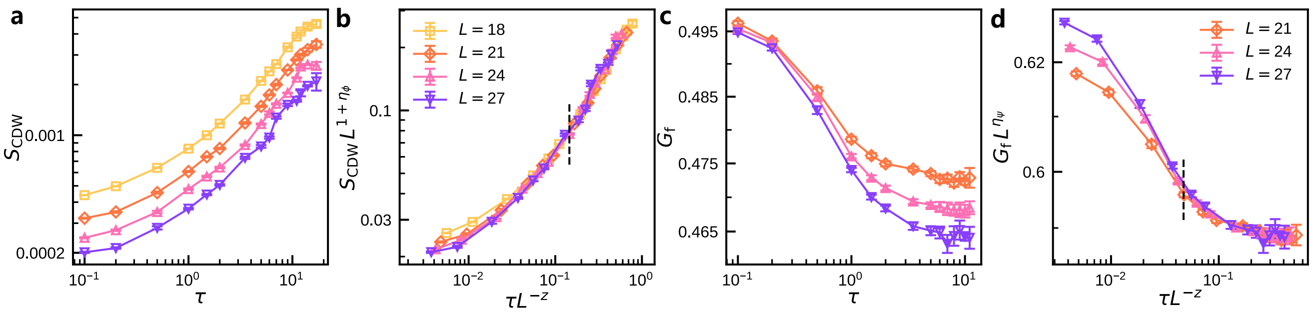

FIG. S10. **Relaxation dynamics at QCP with DSM initial state in spinless t-V model. a-b**, Curves of $S_{\mathrm{CDW}} \equiv S_{\mathrm{CDW}}(\boldsymbol{k} = \mathbf{0})$ versus τ for different sizes before and after rescaling. **c-d**, Curves of $G_{\mathrm{f}} \equiv G_{\mathrm{f}}(\boldsymbol{k} = K + \Delta\boldsymbol{k})$ versus τ before and after rescaling. Data collapse in the relaxation dynamics shows $\eta_\phi = 0.44(2)$ and $\eta_\psi = 0.072(4)$.

and accuracy of our method. More crucially, for the first time, through our method we achieve the reliable result of fermionic anomalous dimension η_ψ for the QCP in the spinless t-V model by unbiased QMC simulation, as shown in Table S2.

TABLE S2. **Comparison of critical properties for the spinless t-V model calculated by different methods.** The method used in this work is the nonequilibrium short-time PQMC.

Methods	U_c	ν	η_ϕ	η_ψ
This work (from CDW, $\tau = 0.3L^z$)	1.35(1)	0.77(12)	0.49(5)	0.073(4)
This work (from DSM, $\tau = 0.3L^z$)	1.37(2)	0.79(5)	0.44(2)	0.072(4)
Majorana QMC (equilibrium) (60)	1.355(1)	0.77(2)	0.45(2)	-
Continuous-time QMC (equilibrium) (59)	1.356(1)	0.80(3)	0.302(7)	-
FRG (58)	-	0.929	0.602	0.069

S4. MORE DETAILS FOR THE SU(3) HUBBARD MODEL

A. SU(3) algebra

The SU(3) Hubbard model with staggered flux is invariant under SU(3) transformations in the flavor space of fermions. Here we give a brief review on the SU(3) algebra.

The generators of the SU(3) group are represented by the well-known Gell-Mann matrices. Below are the eight Gell-Mann matrices, corresponding to the generators of SU(3) group:

$$\lambda_1 = \begin{pmatrix} 0 & 1 & 0 \\ 1 & 0 & 0 \\ 0 & 0 & 0 \end{pmatrix}, \quad \lambda_2 = \begin{pmatrix} 0 & -i & 0 \\ i & 0 & 0 \\ 0 & 0 & 0 \end{pmatrix}, \quad \lambda_3 = \begin{pmatrix} 1 & 0 & 0 \\ 0 & -1 & 0 \\ 0 & 0 & 0 \end{pmatrix},$$
$$\lambda_4 = \begin{pmatrix} 0 & 0 & 1 \\ 0 & 0 & 0 \\ 1 & 0 & 0 \end{pmatrix}, \quad \lambda_5 = \begin{pmatrix} 0 & 0 & -i \\ 0 & 0 & 0 \\ i & 0 & 0 \end{pmatrix}, \quad \lambda_6 = \begin{pmatrix} 0 & 0 & 0 \\ 0 & 0 & 1 \\ 0 & 1 & 0 \end{pmatrix}, \tag{S23}$$
$$\lambda_7 = \begin{pmatrix} 0 & 0 & 0 \\ 0 & 0 & -i \\ 0 & i & 0 \end{pmatrix}, \quad \lambda_8 = \begin{pmatrix} 1/\sqrt{3} & 0 & 0 \\ 0 & 1/\sqrt{3} & 0 \\ 0 & 0 & -2/\sqrt{3} \end{pmatrix}.$$

Note that only λ_8 is full rank, the other seven are not. That is to say, only the order associated with λ_8 can gap out all flavors of fermions.

The Lie algebra structure of the SU(3) group is determined by the commutation relations of its generators. The commutation relations between the generators of the SU(3) group are listed as follows:

$$[\lambda_a, \lambda_b] = 2\mathrm{i} \sum_c f_{abc} \lambda_c, \tag{S24}$$

where f_{abc} are the structure constants, specifically:

$$f_{123} = 1, \tag{S25}$$

$$f_{147} = f_{246} = f_{257} = f_{345} = \frac{1}{2}, \tag{S26}$$

$$f_{156} = f_{367} = -\frac{1}{2}, \tag{S27}$$

$$f_{458} = f_{678} = \frac{\sqrt{3}}{2}. \tag{S28}$$

These commutation relations will determine the manifold shape of the ground-state degeneracy space of the ordered phase, which we will further analyze with numerical evidence in the subsequent sections.

B. Mean-field analyses

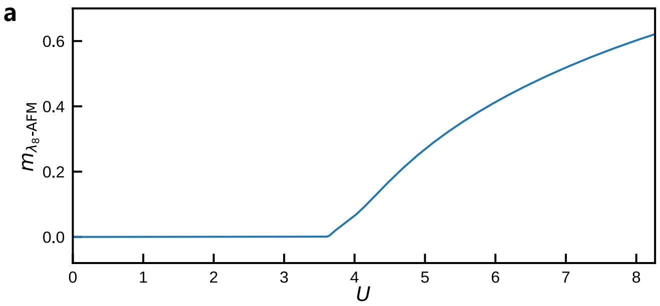

FIG. S11. **Mean-field results for the λ_8-AFM order.** **a**, For $\phi = 0.1\pi, L = 42$, a DSM-AFM transition in the mean-field approximation is seen at $U = 3.637(5)$. **b**, Mean-field phase diagram with $L = 42$.

To qualitatively understand the salient features of ground-state phase diagram and the dominant symmetry spontaneous breaking ordering in the SU(3) Hubbard model, we first perform a mean-field analysis. We rewrite the interaction term in the following form and apply the mean-field approximation:

$$\begin{aligned} \frac{U}{2}\sum_i\left(\sum_\alpha n_{i\alpha} - \frac{3}{2}\right)^2 &= \frac{U}{2}\sum_i\sum_{\alpha,\alpha'} n_{i\alpha}n_{i\alpha'} + \text{const.} \\ &= -\frac{U}{4}\sum_i\sum_{\alpha,\alpha'}\left(n_{i\alpha} - n_{i\alpha'}\right)^2 + \text{const.} \\ &= -\frac{3U}{16}\sum_i\sum_n\left(\boldsymbol{c}_i^\dagger\lambda_n\boldsymbol{c}_i\right)^2 + \text{const.} \\ &\approx -\frac{3U}{16}\sum_n\langle m_{\lambda_n\text{-AFM}}\rangle\sum_i(-1)^i\boldsymbol{c}_i^\dagger\lambda_n\boldsymbol{c}_i + \text{const.}\,, \end{aligned} \tag{S29}$$

where $\boldsymbol{c}_i^\dagger \equiv \left(\boldsymbol{c}_{i1}^\dagger \;\; \boldsymbol{c}_{i2}^\dagger \;\; \boldsymbol{c}_{i3}^\dagger\right)$, and λ_n=$(\lambda_1, \lambda_2, \ldots, \lambda_8)$ are the eight Gell-Mann matrices. The mean-field order parameter is defined as

$$\langle m_{\lambda_n\text{-AFM}} \rangle \equiv \frac{1}{L^2} \sum_i (-1)^i \langle \boldsymbol{c}_i^\dagger \lambda_n \boldsymbol{c}_i \rangle \tag{S30}$$

After applying the mean-field approximation, the Hamiltonian is entirely expressed as a quadratic form of fermionic operators and can be solved for the ground state using exact diagonalization. The problem is then simply reduced to a self-consistent calculation of the order parameter $\{m_{\lambda_n\text{-AFM}}\}$. Fig. S11a shows the variation of the order parameter $m_{\lambda_8\text{-AFM}}$ with interaction strength U calculated using the mean-field method. When the interaction is strong, $m_{\lambda_8\text{-AFM}}$ starts to increase with U, showing clear characteristics of a continuous phase transition. We control different magnetic flux ϕ to find the corresponding phase boundary U, as shown in the mean-field phase diagram in Fig. S11b.

We can understand why the λ_8-AFM order is preferred by examining the ground state energy of the system. Consider placing the eight different order parameter operators in the same external field h:

$$H_n^{\text{sat}} = -h \sum_i (-1)^i \boldsymbol{c}_i^\dagger \lambda_n \boldsymbol{c}_i, \tag{S31}$$

whose ground state corresponds to the saturated λ_n-AFM ordered state. At half-filling, the ground state energy of $H_8^{\text{sat}}(h)$ is $-\frac{2}{\sqrt{3}}hL^2$. The energy gap at half-filling, between the ground state of $H_8^{\text{sat}}(h)$ and the first excited state of $H_8^{\text{sat}}(h)$, is a finite value $\frac{2}{\sqrt{3}}h$. For $H_{n\neq 8}^{\text{sat}}(h)$, the ground state energy is $-hL^2$ and the energy gap is 0. In other words, even considering the saturated ordered state, only the λ_8-AFM order can open a gap in Dirac fermions, while other types of λ_n-AFM cannot.

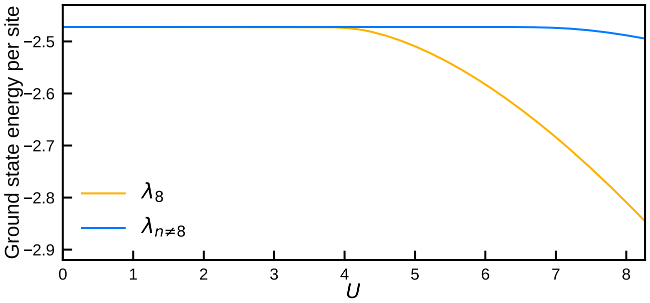

FIG. S12. **Mean-field ground state energy per site at half-filling of different types of λ_n-AFM.** For the mean-field calculation with $\phi = 0.1, L = 42$, the ground state energy of the λ_8-AFM mean-field Hamiltonian is lower than that of other types of Hamiltonians.

Next, we calculate the mean-field ground-state energy for different λ_n-AFM orders. From Fig. S12, we find that λ_8-AFM mean-field states have lower ground-state energy than other types of antiferromagnetic orders in the whole interaction regime of the ordered phases. Thus, from a mean-field perspective, the system favors the λ_8-AFM order.

C. Phase boundary and critical exponents

Here, we perform QMC simulation through short-time relaxation to systematically study the phase boundary and critical properties of the quantum phase transition. To determine the phase boundary of the SU(3) Hubbard model with staggered flux, we compute the structure factor and correlation length ratio. For the λ_8-AFM order, the structure factor is defined as:

$$S_{\lambda_8\text{-AFM}}(\boldsymbol{k}) = \frac{1}{L^{2d}} \sum_{i,j} \mathrm{e}^{\mathrm{i}\boldsymbol{k}\cdot(\boldsymbol{r}_i - \boldsymbol{r}_j)} (-1)^{i+j} \langle \boldsymbol{c}_i^\dagger \lambda_8 \boldsymbol{c}_i \boldsymbol{c}_j^\dagger \lambda_8 \boldsymbol{c}_j \rangle\,, \tag{S32}$$

The associated correlation length ratio is defined as

$$R_{\lambda_8\text{-AFM}} \equiv 1 - \frac{S_{\lambda_8\text{-AFM}}(\boldsymbol{k} = \Delta \boldsymbol{k})}{S_{\lambda_8\text{-AFM}}(\boldsymbol{k} = 0)}. \tag{S33}$$

The fermion correlation $G_{\rm f}(\boldsymbol{k})$ is defined the same as Eq. (S22):

$$G_{\rm f}(\boldsymbol{k}) \equiv \frac{1}{L^2}\sum_{ij} \mathrm{e}^{\mathrm{i}\boldsymbol{k}(\boldsymbol{r}_i-\boldsymbol{r}_j)}\left\langle c^{\dagger}_{i,A}c_{j,B}\right\rangle , \tag{S34}$$

where A, B represent two inequivalent sublattices in a square lattice with staggered flux. In the main text and data figures, unless otherwise specified, we omit the momentum variables and denote $S_{\lambda_8\text{-AFM}} \equiv S_{\lambda_8\text{-AFM}}(\boldsymbol{k}=0)$ and $G_{\rm f} \equiv G_{\rm f}(\boldsymbol{k} = \mathrm{K} + \Delta\boldsymbol{k})$, where $\mathrm{K} = \left(\pm\frac{\pi}{2}, \pm\frac{\pi}{2}\right)$ represents the momentum at the Dirac points.

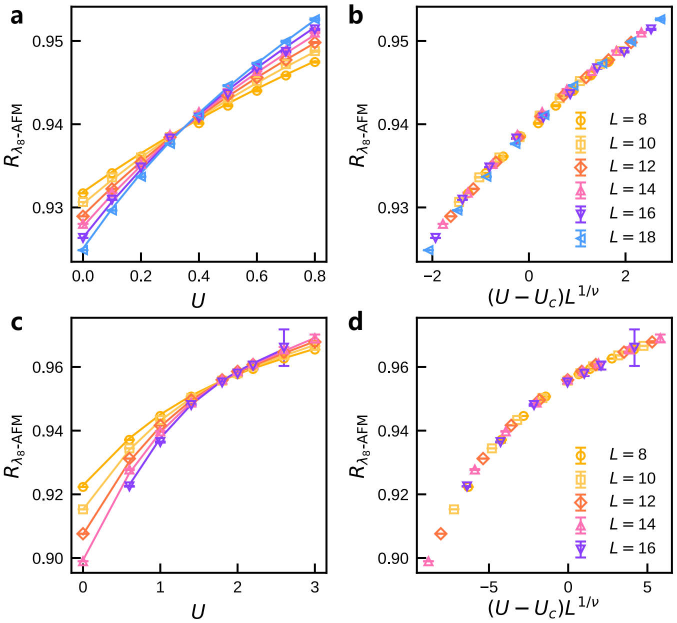

FIG. S13. **Curves of $R_{\lambda_8\text{-AFM}}$ versus U for different sizes with λ_8-AFM initial state at $\tau = 0.25L^z$. a-b**, For $\phi = 0.05\pi$, the fitted critical point is $U_c = 0.347(4)$, with the critical exponent $1/\nu = 0.67(1)$. **c-d**, For $\phi = 0.1\pi$, the fitted critical point is $U_c = 2.0(3)$, with $1/\nu = 0.58(7)$.

To identify phase boundary between the DSM phase and the λ_8-AFM phase, we prepare a λ_8-AFM initial state and calculate the critical point for fixed ϕ by the method of short-time dynamics. For fixed $\tau L^{-z} = 0.25$. We calculate the critical point for $\phi = 0.05\pi$, $\phi = 0.075\pi$ and 0.1π by the intersection points of curves of $R_{\lambda_8\text{-AFM}}$ versus U for different L. As shown in Fig. S13, critical points are $U_c = 0.347(4)$ for $\phi = 0.05\pi$, $U_c = 2.0(3)$ for $\phi = 0.1\pi$, and $U_c = 1.10(5)$ for $\phi = 0.075\pi$ as shown in the main text.

Here, to further confirm the λ_8-AFM is the dominant ordering, we also compute the correlation length ratio for other quantities. We find that there is no crossing in the curves of $R_{\lambda_n\text{-AFM}}$ for the AFM orders defined by λ_1 to λ_7 versus U, as shown in Fig. S14. The results of the correlation length ratio decrease with L, demonstrating the absence of long-range order. Hence, the λ_8-AFM is the dominant ordering, and other AFM orders are all short-range in the half-filled SU(3) Hubbard model with staggered flux.

Moreover, scaling collapse for the curves of $R_{\lambda_8\text{-AFM}}$ versus rescaled $(U - U_c)$ gives the value of $1/\nu$. Accordingly, we obtain $1/\nu = 0.67(1)$ and $1/\nu = 0.58(7)$ for $\phi = 0.05\pi$ and $\phi = 0.1\pi$, respectively. Combining $1/\nu = 0.68(5)$ with $\phi = 0.075\pi$ shown in the main text, we find that the values of $1/\nu$ are consistent with each other within error bar, showing the universality of the quantum phase transition between DSM and λ_8-AFM ordered phase.

To determine the anomalous dimensions η_ϕ and η_ψ of the bosonic field and the fermionic field we study the relaxation dynamics of the structure factor $S_{\lambda_8\text{-AFM}} = S_{\lambda_8\text{-AFM}}(\boldsymbol{k} = 0)$ and the fermion correlation $G_{\rm f} = G_{\rm f}(\boldsymbol{k} = \mathrm{K} + \Delta\boldsymbol{k})$ at the critical point. The curves before and after rescaling are shown in Figs. S15 and S16 and Fig. 3 in the main text for different ϕ. The critical exponents determined above are summarized in Table S3, from which we find that the anomalous dimensions for different ϕ are consistent with each other within error bar, further confirming the universality of the phase transition.

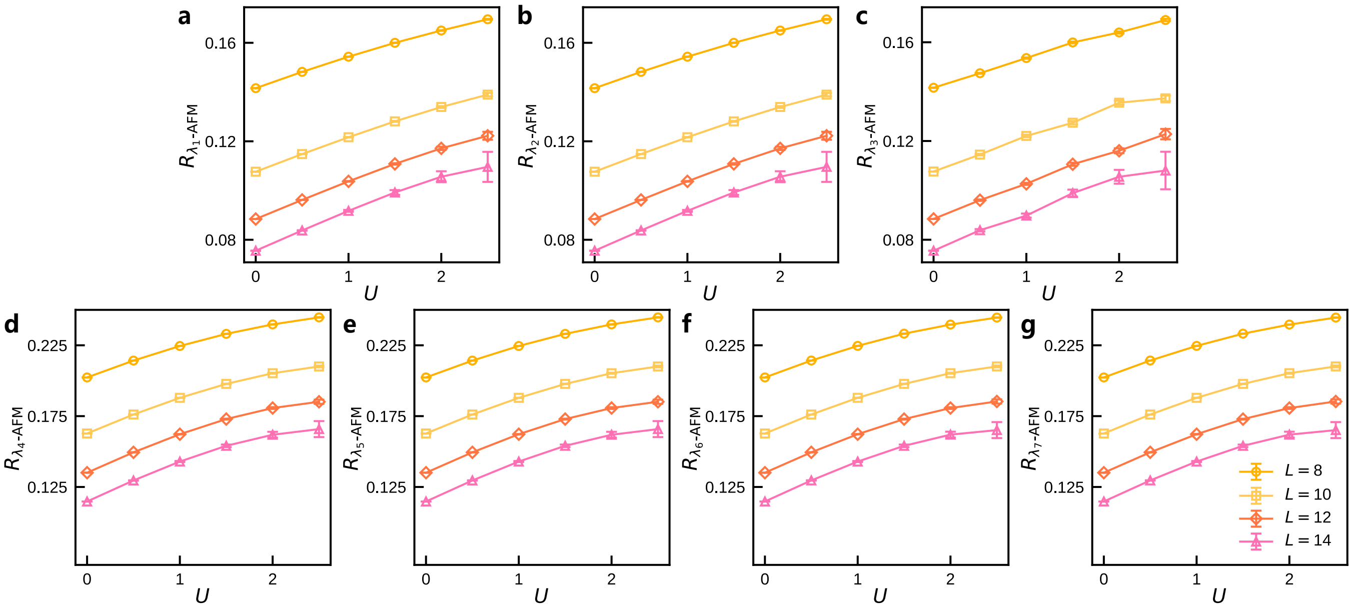

FIG. S14. **Correlation length ratios for λ_1-AFM to λ_7-AFM versus U for different sizes with λ_8-AFM initial state at $\tau = 0.25L^z, \phi = 0.075\pi$.** There is no crossing point in the curves of $R_{\lambda_n\text{-AFM}}$ versus U.

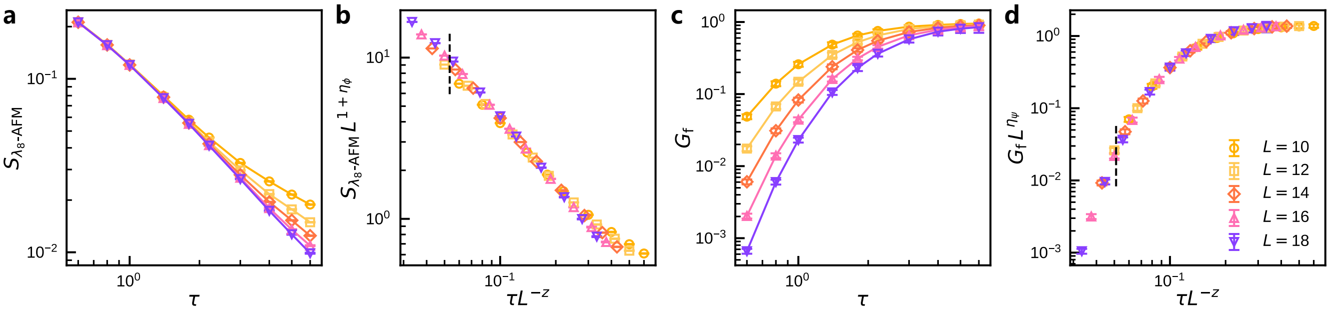

FIG. S15. **Relaxation dynamics at the QCP $\phi = 0.05\pi, U = 0.347(4)$ with λ_8-AFM initial state in SU(3) Hubbard model. a-b**, Curves of S versus τ for different sizes before and after rescaling. **c-d**, Curves of G versus τ before and after rescaling. Data collapse in the relaxation dynamics shows $\eta_\phi = 0.51(3)$ and $\eta_\psi = 0.16(2)$.

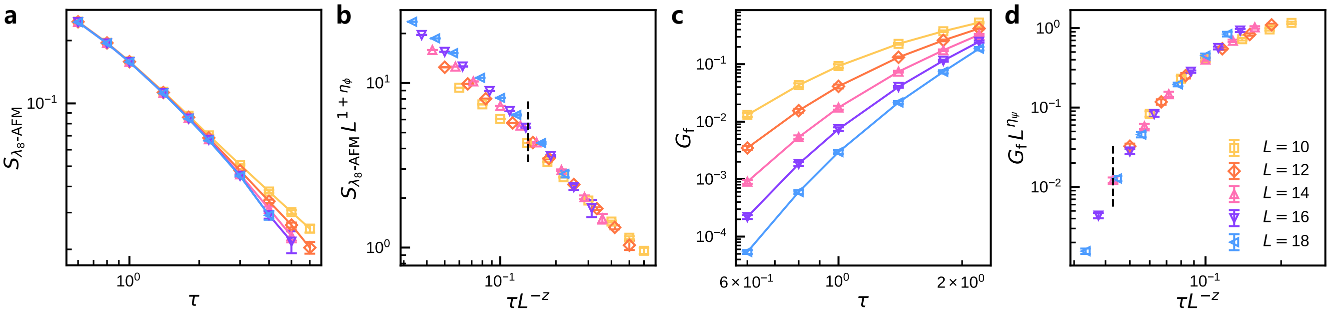

FIG. S16. **Relaxation dynamics at the QCP $\phi = 0.1\pi, U = 2.0(3)$ with λ_8-AFM initial state in SU(3) Hubbard model. a-b**, Curves of S versus τ for different sizes before and after rescaling. **c-d**, Curves of G versus τ before and after rescaling. Data collapse in the relaxation dynamics shows $\eta_\phi = 0.58(10)$ and $\eta_\psi = 0.16(3)$.

TABLE S3. **Critical properties for the SU(3) Hubbard model probed under different staggered flux ϕ.**

$\boldsymbol{\phi}$	$\boldsymbol{U_c}$	$\boldsymbol{\nu^{-1}}$	$\boldsymbol{\eta_\phi}$	$\boldsymbol{\eta_\psi}$
0.05π	0.347(4)	0.67(1)	0.51(3)	0.16(2)
0.075π	1.10(5)	0.68(5)	0.55(5)	0.15(3)
0.1π	2.0(3)	0.58(7)	0.58(10)	0.16(3)

D. The new universality class

In three-dimensional classical systems or 2+1 dimensional quantum systems, the most typical O(N) universality classes widely describe a variety of important phase transitions, such as the gas-liquid transition of simple gases, the superfluid transition of liquid helium, and the Heisenberg transition of ferromagnets. Specifically, the $N = 1$ case is referred to as the Ising universality class, $N = 2$ as the XY universality class, and $N = 3$ as the Heisenberg universality class. Their critical behaviors can be simply described by purely bosonic ϕ^4 theories with O(N) symmetries.

When the boson order parameter fields are coupled to Dirac fermions, the critical properties are significantly modified by the gapless fermion fluctuations, which leads to the definition of the "chiral versions" of the above universality classes (73), namely the *O(N_b)* universality classes. To avoid confusion, we here use N to denote the dimension of the classical order parameter, N_{b} to denote the dimension of the bosonic order parameter, and N_{f} to denote the number of fermion flavors. For example, quantum phase transitions with a Z_2 charge-density-wave order parameter belong to the *chiral Ising* universality class; those with an O(2), or equivalently U(1), superconducting order parameter belong to the *chiral XY* universality class; and those with an O(3) antiferromagnetic order parameter belong to the *chiral Heisenberg* universality class. The corresponding low-energy effective field theories at criticality are obtained by coupling the ϕ^4 bosonic theory of the order parameter to chiral fermion fields through Yukawa terms, and can generally be written as

$$\mathcal{L} = \mathrm{tr}\big(\bar{\psi}\not{\partial}\psi\big) + g\,\mathrm{tr}\big(\bar{\psi}\Phi\psi\big) + \mathrm{tr}\big((\partial_\mu\Phi)^2\big) + r\,\mathrm{tr}\big(\Phi^2\big) + \lambda\left(\mathrm{tr}(\Phi^2)\right)^2 , \tag{S35}$$

where ψ is the fermion spinor field, and tr denotes the trace over the N_{f} flavors of chiral fermions with SU(N_{f}) symmetry. The operator $\Phi = \sum_{i=1}^{N_{\mathrm{b}}} \phi_i L_i$ spans an N_{b}-dimensional linear representation of the SU(N_{f}) algebra, with N_{b} linearly independent bosonic components, and the N_{f}-dimensional matrices L_i form an orthogonal basis of this representation, such that $\mathrm{tr}(\Phi^2) = \sum_{i=1}^{N_{\mathrm{b}}} \phi_i^2$. This theory is the well-known Gross-Neveu-Yukawa theory. Therefore, these chiral O(N_{b}) universality classes are collectively referred to as the *Gross-Neveu universality classes*. Their order parameters correspond to the N_{b}-dimensional real linear representation of the fermionic SU(2) algebra, which happens to carry a faithful representation of the O(N_{b}) group. Consequently, the bosonic fields in the theory also possess O(N_{b}) symmetry, establishing a one-to-one correspondence with the usual O(N) universality classes. For instance, for the $N_{\mathrm{b}} = 3$ chiral Heisenberg universality class in an SU($N_{\mathrm{f}} = 2$) system, Eq. (S35) can be written in the more familiar form

$$\mathcal{L} = \bar{\psi}\not{\partial}\psi + g\,\bar{\psi}\left(\vec{\phi}\cdot\vec{\sigma}\right)\psi + \left|\partial_\mu\vec{\phi}\right|^2 + r\left|\vec{\phi}\right|^2 + \lambda\left|\vec{\phi}\right|^4 , \tag{S36}$$

where $\vec{\phi} = (\phi_1, \phi_2, \phi_3)$ is an O(3) vector and $\vec{\sigma} = (\sigma_x, \sigma_y, \sigma_z)$ are the Pauli matrices, forming an orthogonal basis for the three-dimensional linear representation of the SU(2) algebra. We summarize in Table S4 the theoretical symmetries and the vacuum manifolds (ground-state degeneracy manifolds) after spontaneous symmetry breaking corresponding to various chiral O(N_{b}) universality classes.

The Gross-Neveu universality class describes the universal physics in which massless Dirac fermions acquire a mass through spontaneous symmetry breaking. Although the known Gross-Neveu universality classes possess an O(N) order-parameter structure, considering the intrinsic spinor nature of fermions, the Gross-Neveu universality class should not simply be regarded as the chiral counterpart of the classical O(N) universality class. A fundamental question of broad interest across statistical physics, condensed matter physics, and high-energy physics is whether fermionic Gross-Neveu criticality can arise that goes beyond the O(N) counterparts.

We find that SU(N_{f}) Dirac fermion systems with with odd N_{f} offer precisely such a pathway. From the perspective of the structure of symmetry group algebras, the key distinction between odd and even N_{f} lies in the fact that SU(N_{f}) groups with odd N_{f} cannot be isomorphic to spin groups, which may allow for the emergence of "more fermionic" universality classes, as illustrated in Fig S17. For even N_{f}, however, at small values of N_{f}, such as SU(2) and SU(4), the groups are locally isomorphic to O(3) and O(6), respectively; while at large N_{f}, the system typically does not favor breaking SU(N_{f}) symmetry to form spin order, but instead tends to form a valence-bond solid (81, 82).

TABLE S4. Comparison of the symmetries of different Gross-Neveu universality classes. The symmetries of the theories and the vacuum manifolds (ground-state degeneracy manifolds) after spontaneous symmetry breaking are listed. Each chiral $\mathrm{O}(N_\mathrm{b})$ universality class corresponds to an $\mathrm{O}(N)$ universality class with the same symmetries and vacuum manifold. In contrast, the new chiral SU(3) universality class reported in our manuscript has no corresponding $\mathrm{O}(N)$ universality class.

Gross-Neveu classes		Symmetry		Vacuum manifold
chiral $\mathrm{O}(N_\mathrm{b})$	chiral Ising	$\mathrm{O}(N_\mathrm{b})$	Z_2, $N_\mathrm{b}=1$	S^0
	chiral XY		$O(2)$, $N_\mathrm{b}=2$	S^1
	chiral Heisenberg		$O(3)$, $N_\mathrm{b}=3$	S^2
chiral SU(3)		$\mathrm{SU}(3)\times\mathrm{Z}_2$		$\frac{\mathrm{SU}(3)\times\mathrm{Z}_2}{\mathrm{SU}(2)\times\mathrm{U}(1)}$ $(\simeq \mathbb{CP}^2\times\mathrm{Z}_2)$

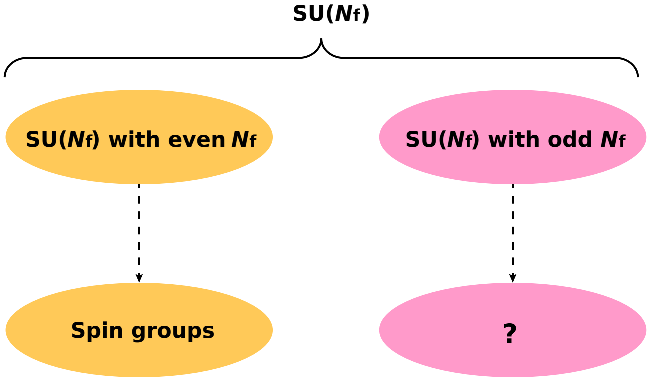

FIG. S17. For odd N_f, the $\mathrm{SU}(N_\mathrm{f})$ group cannot be isomorphic to a spin group, which may give rise to new Gross-Neveu universality classes that more directly manifest the spinor nature of fermions.

Indeed, all Gross-Neveu transitions studied so far for even N_f fall back into the conventional chiral $\mathrm{O}(N_\mathrm{b})$ universality classes (83-88). Therefore, investigating the case of odd N_f is of fundamental importance for understanding fermionic phase transitions.

We clearly identify the first nontrivial fermionic Gross-Neveu criticality that goes beyond the $\mathrm{O}(N)$ order-parameter structures. The continuous transition from the SU(3) DSM to the λ_8-AFM phase reported in our manuscript belongs to the Gross-Neveu universality class family but does not fall into any of the known chiral Ising, chiral XY, or chiral Heisenberg classes.

In the saturated λ_8-AFM phase, two flavors of fermions (referred to as flavors 1 and 2) are localized in one sublattice (designated as the A lattice), while the remaining flavor of fermions (referred to as flavor 3) is localized in the other sublattice (designated as the B lattice), as illustrated in Fig. 3a of the main text. It is evident that the Z_2 symmetry between the AB sublattices is significantly broken. The diagonal λ_8 generator induces a global U(1) transformation, while the generators $\lambda_1, \lambda_2, \lambda_3$ act solely on the subspace of flavors 1 and 2, generating a closed SU(2) transformation that only mixes these two flavors. Since these four generators all commute with the order parameter operator, the $\mathrm{SU}(2)\times\mathrm{U}(1)$ is the largest symmetry group that remains invariant under the λ_8-AFM order parameter after spontaneous symmetry breaking. The other four generators of the SU(3) group, $\lambda_4, \lambda_5, \lambda_6, \lambda_7$, produce transformations that alter the direction of the AFM order parameter $\{m_n\}$ in a compact manifold, leading to other λ_8-AFM degenerate ground states, which are four independent Goldstone modes. All degenerate ground states span a 4-dimensional ground state degeneracy space, and these states can be mapped one-to-one onto points on the manifold $\frac{\mathrm{SU}(3)\times\mathrm{Z}_2}{\mathrm{SU}(2)\times\mathrm{U}(1)}$. Under SU(3) transformations, this order parameter transforms according to the 8-dimensional adjoint representation of SU(3) and spans the 4-dimensional $\frac{\mathrm{SU}(3)\times\mathrm{Z}_2}{\mathrm{SU}(2)\times\mathrm{U}(1)}$ manifold, which is nonlinearly embedded in $\mathbb{R}^8$. SU(3) cannot be isomorphic or locally isomorphic to any other classical linear groups, which is in sharp contrast to the cases of even N_f such as SU(2) and SU(4). Therefore, the new SU(3) antiferromagnetic order parameter we have discovered does not have a corresponding $\mathrm{O}(N_\mathrm{b})$ order parameter. We temporarily refer to this new universality class as the *chiral SU(3)* universality class. As shown in the comparison in Table S4 summarizes the differences of this new universality class from the previously known ones in terms of symmetry and vacuum manifold. In addition to the symmetry analysis, our QMC results also provide an unbiased numerical determination of the critical exponents of this new universality class. In Table S5, we present a comparison of its critical exponents with those of the chiral

TABLE S5. **Comparison of critical exponents for different Gross-Neveu-Yukawa universality classes in $d = 2+1$ with $N_{\mathrm{f}} = 6$.** The first row, chiral SU(3) denotes the universality class for SU(3) Dirac fermion Hubbard model, with exponents determined from nonequilibrium PQMC.

Universality class	$\boldsymbol{\nu^{-1}}$	$\boldsymbol{\eta_\phi}$	$\boldsymbol{\eta_\psi}$
chiral SU(3) (this work)	0.68(5)	0.55(5)	0.15(3)
chiral Heisenberg ($4-\epsilon$, 2nd order)(73)	1.478	1.023	0.058
chiral XY ($4-\epsilon$, 2nd order)(73)	1.809	0.698	0.082
chiral Ising ($4-\epsilon$, 2nd order)(73)	0.750	0.865	0.011
chiral Ising (FRG)(74)	0.993	0.912	0.013

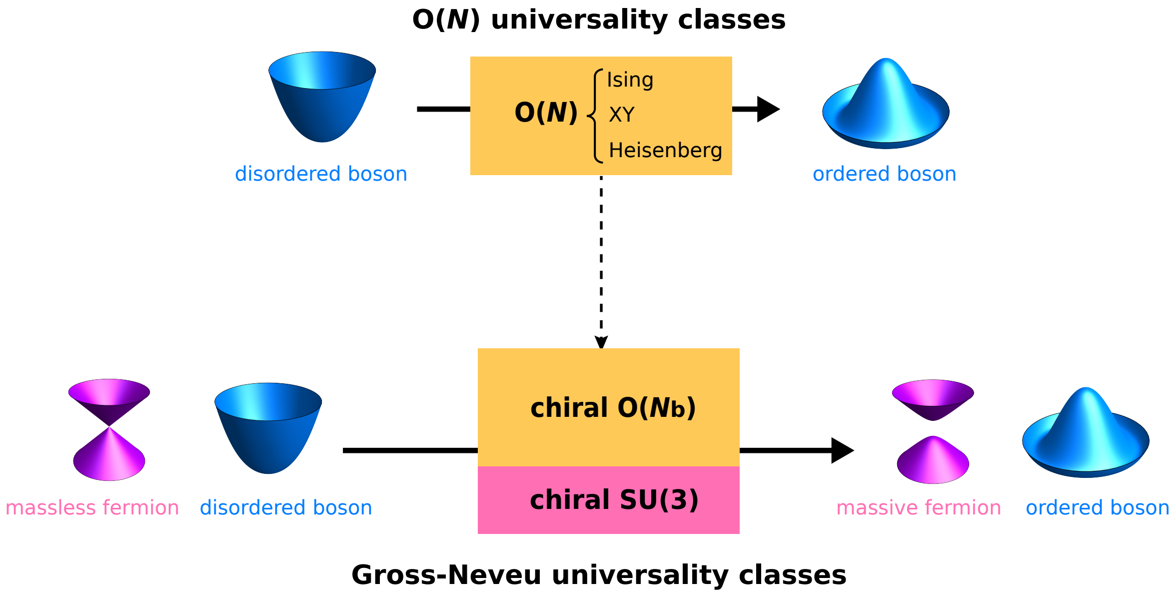

FIG. S18. Schematic illustration of the relationship between O(N) universality classes and Gross-Neveu universality classes. The O(N) universality classes, including Ising, Heisenberg, and XY, describe spontaneous symmetry breaking with an O(N) order parameter. The Gross-Neveu universality classes describe the situation where, along with spontaneous symmetry breaking of the bosonic order parameter, massless Dirac fermions also spontaneously acquire a mass. Within the Gross-Neveu universality classes, the traditional chiral O(N) universality classes correspond one-to-one to the O(N) universality classes, whereas the chiral SU(3) universality class in the Gross-Neveu universality classes does not possess an O(N) order-parameter structure and instead represents a fermion-intrinsic universality class.

Ising, chiral XY, and chiral Heisenberg universality classes, which more conclusively rules out the possibility that this new universality class belongs to those existing universality classes.

The nontrivial new Gross-Neveu universality class we discovered represents the first minimal example of a Gross-Neveu transition without a classical O(N) correspondence. As illustrated in Fig. S18, our results demonstrate that the Gross-Neveu universality class encompasses a broader and nontrivial set with intrinsic fermionic characteristics. It is highly worthwhile in the future to further investigate the low-energy effective field theory of this phase transition. Since the bosonic field does not possess O(N_{b}) symmetry, its form is likely different from the previous expression in Eq. (S35). We conjecture that it may take the following form:

$$\mathcal{L} = \mathrm{tr}\left(\bar{\psi}\not{\partial}\psi\right) + g\,\mathrm{tr}\left(\bar{\psi}\Phi\psi\right) + \mathrm{tr}\left[\left(\partial_\mu\Phi\right)^2\right] + r\,\mathrm{tr}\left(\Phi^2\right) + \lambda\left[\mathrm{tr}\left(\Phi^2\right)\right]^2 + a\left[\mathrm{tr}\left(\Phi^3\right)\right]^2 + c\left[\mathrm{tr}\left(\Phi^2\right)\right]^4, \tag{S37}$$

where $\Phi = \sum_{i=1}^{N_{\mathrm{b}}} \phi_i \frac{\lambda_i}{2}$, $N_{\mathrm{b}} = 8$ spans the 8-dimensional adjoint representation of SU(3). Compared with Eq. (S35), the marginal term $a\left[\mathrm{tr}\left(\Phi^3\right)\right]^2$ is introduced to reduce the SO(8) symmetry of the bosonic field to $\mathrm{SU}(3) \times \mathrm{Z}_2$ symmetry, while the irrelevant term $c\left[\mathrm{tr}\left(\Phi^2\right)\right]^4$ with $c > 0$ is also introduced to ensure vacuum stability. Due to the SU(3) algebra identity $\mathrm{tr}(\Phi^3) = 3\det\Phi$, only the ϕ_8 component of the order parameter along the λ_8 direction with full rank contributes a nonzero value to $\left[\mathrm{tr}\left(\Phi^3\right)\right]^2$. Therefore, when $a < 0$, the SU(3)-symmetric bosonic field tends to spontaneously break toward the λ_8 direction. This is very different from the $\mathrm{O}(N)$ symmetry breaking triggered by $r < 0$ in the ϕ^4 theory. Whether such a Gross-Neveu-Yukawa theory can capture the new universality class we discovered (for example, yielding critical exponents consistent with our numerical results) remains an open question for future study. Additionally, such an order parameter that carries an SU(3) bilinear representation rather than an $\mathrm{O}(N_\mathrm{b})$ linear representation may also be constructed through a recent theoretical framework with tensorial criticality (89-91), which is also worth exploring.

E. Sign problem behaviors and computational efficiency

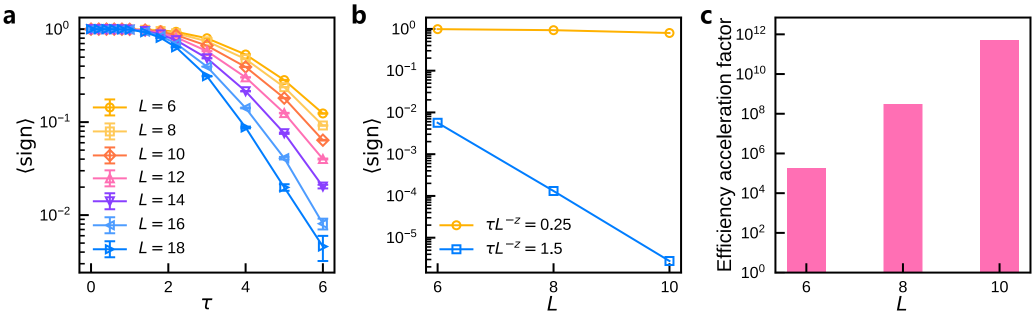

FIG. S19. **The sign problem in SU(3) Hubbard model at the QCP $\phi = 0.1, U = 2.0(3)$.** **a**, The average sign with different L and τ in short-time stage. **b**, Comparison for the average sign between short-time stage ($\tau = 0.25L^z$) and equilibrium stage ($\tau = 1.5L^z$). **c**, Efficiency gain of QMC with the short-time method ($\tau = 0.25L^z$) compared to equilibrium QMC ($\tau = 1.5L^z$) for different sizes L.

For this model, we set the parameters at the critical point $U = 2.0(3)$, $\phi = 0.1\pi$. The average sign as a function of imaginary time τ and size L is shown in Fig. S19a. The sign problem for this model is significantly more severe than for the previous two models. For $\tau = 0.25L^z$, the average sign is approximately $10^{-1} \sim 10^{-2}$, meaning that compared to the sign-problem-free case, 10 to 100 times more computational resources are needed to obtain reliable results. From Figs. S15 and S16 and Fig. 3 in the main text, it can be seen that $\tau = 0.25L^z$ is in the nonequilibrium scaling region controlled by the critical point. Even though the ground state is not reached, its nonequilibrium scaling still reflects the quantum criticality of the ground state. In equilibrium QMC studies, it is typically necessary to set the imaginary time τ to more than 1.5 times the size L^z to reach the ground state. However, evolving for such a long time, the average sign decays to approximately $10^{-5} \sim 10^{-6}$. In Fig. S19b, we compare the average sign for $\tau = 0.25L^z$ and $\tau = 1.5L^z$. Since the computational error (according to Eq. S8) is inversely proportional to the average sign $\langle\mathrm{sign}\rangle$ (according to Eq. S8), we can measure the difference in computational efficiency by multiplying the ratio of the average sign $\langle\mathrm{sign}\rangle$ by the length of imaginary-time evolution, as follows:

$$\text{Efficiency acceleration factor} = \left(\frac{1/\left\langle\mathrm{sign}\right\rangle_{\mathrm{eq.}}}{1/\left\langle\mathrm{sign}\right\rangle_{\mathrm{neq.}}}\right)^2 \frac{\tau_{\mathrm{eq.}}}{\tau_{\mathrm{neq.}}}, \tag{S38}$$

where the nonequilibrium evolution time is $\tau_{\mathrm{neq.}} = 0.25L^z$, and the equilibrium evolution time is $\tau_{\mathrm{eq.}} = 1.5L^z$. $\langle\mathrm{sign}\rangle_{\mathrm{neq.}}$ and $\langle\mathrm{sign}\rangle_{\mathrm{eq.}}$ are their corresponding average signs, as shown in Fig. S19b. We specifically compared the differences in computational efficiency for several system sizes, as shown in Fig. S19c. The computational resources required by the nonequilibrium method are only a few millionths of those required by the equilibrium method, and this efficiency improvement roughly grows exponentially with the system size. Consequently, our nonequilibrium method enables the QMC simulation on SU(3) Hubbard model with large system size, which is not accessible in previous unbiased numerical approaches.

REFERENCES

1. S. Sachdev, *Quantum Phase Transitions* (Cambridge Univ. Press, ed. 2, 2011); https://doi.org/10.1017/CBO9780511973765.

2. J. Zaanen, Quantum critical electron systems: The uncharted sign worlds. *Science* **319**, 1205–1207 (2008).

3. S. Weinberg, *The Quantum Theory of Fields* (Cambridge Univ. Press, 2013), vol. 1.

4. R. Blankenbecler, D. J. Scalapino, R. L. Sugar, Monte Carlo calculations of coupled boson-fermion systems. I. *Phys. Rev. D* **24**, 2278–2286 (1981).

5. J. E. Hirsch, D. J. Scalapino, R. L. Sugar, R. Blankenbecler, Efficient Monte Carlo procedure for systems with fermions. *Phys. Rev. Lett.* **47**, 1628–1631 (1981).

6. J. E. Hirsch, Two-dimensional Hubbard model: Numerical simulation study. *Phys. Rev. B* **31**, 4403–4419 (1985).

7. E. Y. Loh, J. E. Gubernatis, R. T. Scalettar, S. R. White, D. J. Scalapino, R. L. Sugar, Sign problem in the numerical simulation of many-electron systems. *Phys. Rev. B* **41**, 9301–9307 (1990).

8. P. Henelius, A. W. Sandvik, Sign problem in Monte Carlo simulations of frustrated quantum spin systems. *Phys. Rev. B* **62**, 1102–1113 (2000).

9. M. Troyer, U.-J. Wiese, Computational complexity and fundamental limitations to fermionic quantum Monte Carlo simulations. *Phys. Rev. Lett.* **94**, 170201 (2005).

10. M. B. Hastings, How quantum are non-negative wavefunctions? *J. Math. Phys.* **57**, 015210 (2016).

11. Z. Ringel, D. L. Kovrizhin, Quantized gravitational responses, the sign problem, and quantum complexity. *Sci. Adv.* **3**, e1701758 (2017).

12. D. P. Arovas, E. Berg, S. A. Kivelson, S. Raghu, The Hubbard model. *Annu. Rev. Condens. Matter Phys.* **13**, 239–274 (2022).

13. M. Qin, T. Schäfer, S. Andergassen, P. Corboz, E. Gull, The Hubbard model: A computational perspective. *Annu. Rev. Condens. Matter Phys.* **13**, 275–302 (2022).

14. T. DeGrand, C. DeTar, *Lattice Methods for Quantum Chromodynamics* (World Scientific, 2006); https://doi.org/10.1142/6065.

15. Z.-X. Li, H. Yao, Sign-problem-free fermionic quantum Monte Carlo: Developments and applications. *Annu. Rev. Condens. Matter Phys.* **10**, 337–356 (2019).

16. S. Chandrasekharan, U.-J. Wiese, Meron-cluster solution of fermion sign problems. *Phys. Rev. Lett.* **83**, 3116–3119 (1999).

17. E. F. Huffman, S. Chandrasekharan, Solution to sign problems in half-filled spin-polarized electronic systems. *Phys. Rev. B* **89**, 111101 (2014).

18. C. Wu, S.-C. Zhang, Sufficient condition for absence of the sign problem in the fermionic quantum Monte Carlo algorithm. *Phys. Rev. B* **71**, 155115 (2005).

19. E. Berg, M. A. Metlitski, S. Sachdev, Sign-problem-free quantum Monte Carlo of the onset of antiferromagnetism in metals. *Science* **338**, 1606–1609 (2012).

20. Z.-X. Li, Y.-F. Jiang, H. Yao, Solving the fermion sign problem in quantum Monte Carlo simulations by Majorana representation. *Phys. Rev. B* **91**, 241117 (2015).

21. Z.-X. Li, Y.-F. Jiang, H. Yao, Majorana-time-reversal symmetries: A fundamental principle for sign-problem-free quantum Monte Carlo simulations. *Phys. Rev. Lett.* **117**, 267002 (2016).

22. S. Zhang, H. Krakauer, Quantum Monte Carlo method using phase-free random walks with slater determinants. *Phys. Rev. Lett.* **90**, 136401 (2003).

23. L. Wang, Y.-H. Liu, M. Iazzi, M. Troyer, G. Harcos, Split orthogonal group: A guiding principle for sign-problem-free fermionic simulations. *Phys. Rev. Lett.* **115**, 250601 (2015).

24. Z. C. Wei, C. Wu, Y. Li, S. Zhang, T. Xiang, Majorana positivity and the fermion sign problem of quantum Monte Carlo simulations. *Phys. Rev. Lett.* **116**, 250601 (2016).

25. R. Mondaini, S. Tarat, R. T. Scalettar, Quantum critical points and the sign problem. *Science* **375**, 418–424 (2022).

26. D. Hangleiter, I. Roth, D. Nagaj, J. Eisert, Easing the Monte Carlo sign problem. *Sci. Adv.* **6**, eabb8341 (2020).

27. R. Levy, B. K. Clark, Mitigating the sign problem through basis rotations. *Phys. Rev. Lett.* **126**, 216401 (2021).

28. Z.-Y. Han, Z.-Q. Wan, H. Yao, Pfaffian quantum Monte Carlo: Solution to Majorana sign ambiguity and applications. arXiv:2408.10311 [cond-mat.str-el] (2024).

29. A. Alexandru, G. Başar, P. F. Bedaque, N. C. Warrington, Complex paths around the sign problem. *Rev. Mod. Phys.* **94**, 015006 (2022).

30. O. Golan, A. Smith, Z. Ringel, Intrinsic sign problem in fermionic and bosonic chiral topological matter. *Phys. Rev. Res.* **2**, 043032 (2020).

31. W.-X. Chang, Z.-X. Li, Boosting quantum Monte Carlo and alleviating sign problem by gutzwiller projection. *Phys. Rev. B* **110**, 085152 (2024).

32. Z.-Q. Wan, S.-X. Zhang, H. Yao, Mitigating the fermion sign problem by automatic differentiation. *Phys. Rev. B* **106**, L241109 (2022).

33. X. Zhang, G. Pan, X. Y. Xu, Z. Y. Meng, Fermion sign bounds theory in quantum Monte Carlo simulation. *Phys. Rev. B* **106**, 035121 (2022).

34. T. Sato, F. F. Assaad, Quantum Monte Carlo simulation of generalized kitaev models. *Phys. Rev. B* **104**, L081106 (2021).

35. M.-S. Vaezi, A.-R. Negari, A. Moharramipour, A. Vaezi, Amelioration for the sign problem: An adiabatic quantum Monte Carlo algorithm. *Phys. Rev. Lett.* **127**, 217003 (2021).

36. O. Grossman, E. Berg, Robust fermi-liquid instabilities in sign problem-free models. *Phys. Rev. Lett.* **131**, 056501 (2023).

37. S. L. Sondhi, S. M. Girvin, J. P. Carini, D. Shahar, Continuous quantum phase transitions. *Rev. Mod. Phys.* **69**, 315–333 (1997).

38. M. Vojta, Quantum phase transitions. *Rep. Prog. Phys.* **66**, 2069–2110 (2003).

39. J. A. Hertz, Quantum critical phenomena. *Phys. Rev. B* **14**, 1165–1184 (1976).

40. A. J. Millis, Effect of a nonzero temperature on quantum critical points in itinerant fermion systems. *Phys. Rev. B* **48**, 7183–7196 (1993).

41. E. Berg, S. Lederer, Y. Schattner, S. Trebst, Monte Carlo studies of quantum critical metals. *Annu. Rev. Condens. Matter Phys.* **10**, 63–84 (2019).

42. D. J. Scalapino, A common thread: The pairing interaction for unconventional superconductors. *Rev. Mod. Phys.* **84**, 1383–1417 (2012).

43. P. A. Lee, N. Nagaosa, X.-G. Wen, Doping a mott insulator: Physics of high-temperature superconductivity. *Rev. Mod. Phys.* **78**, 17–85 (2006).

44. S. Lederer, Y. Schattner, E. Berg, S. A. Kivelson, Enhancement of superconductivity near a nematic quantum critical point. *Phys. Rev. Lett.* **114**, 097001 (2015).

45. C. M. Varma, Colloquium: Linear in temperature resistivity and associated mysteries including high temperature superconductivity. *Rev. Mod. Phys.* **92**, 031001 (2020).

46. P. W. Phillips, N. E. Hussey, P. Abbamonte, Stranger than metals. *Science* **377**, eabh4273 (2022).

47. H. K. Janssen, B. Schaub, B. Schmittmann, New universal short-time scaling behaviour of critical relaxation processes. *Z. Phys. B Condens. Matter* **73**, 539–549 (1989).

48. Z. B. Li, L. Schülke, B. Zheng, Dynamic Monte Carlo measurement of critical exponents. *Phys. Rev. Lett.* **74**, 3396–3398 (1995).

49. S. Yin, P. Mai, F. Zhong, Universal short-time quantum critical dynamics in imaginary time. *Phys. Rev. B* **89**, 144115 (2014).

50. Y.-K. Yu, Z. Zeng, Y.-R. Shu, Z.-X. Li, S. Yin, Nonequilibrium dynamics in Dirac quantum criticality. arXiv:2310.10601 [cond-mat.str-el] (2023).

51. F. Assaad, H. Evertz, *World-Line and Determinantal Quantum Monte Carlo Methods for Spins, Phonons and Electrons* (Springer, 2008), pp. 277–356.

52. V. I. Iglovikov, E. Khatami, R. T. Scalettar, Geometry dependence of the sign problem in quantum Monte Carlo simulations. *Phys. Rev. B* **92**, 045110 (2015).

53. S. Sorella, S. Baroni, R. Car, M. Parrinello, A novel technique for the simulation of interacting fermion systems. *Europhys. Lett.* **8**, 663–668 (1989).

54. S. Sorella, The Hubbard-stratonovich transformation and the Hubbard model. *Int. J. Mod. Phys. B* **5**, 937–976 (1991).

55. S. M. Tabatabaei, A.-R. Negari, J. Maciejko, A. Vaezi, Chiral ising gross-neveu criticality of a single Dirac cone: A quantum Monte Carlo study. *Phys. Rev. Lett.* **128**, 225701 (2022).

56. Z.-X. Li, A. Vaezi, C. B. Mendl, H. Yao, Numerical observation of emergent spacetime supersymmetry at quantum criticality. *Sci. Adv.* **4**, eaau1463 (2018).

57. T. C. Lang, A. M. Läuchli, Quantum Monte Carlo simulation of the chiral Heisenberg Gross-Neveu-Yukawa phase transition with a single Dirac cone. *Phys. Rev. Lett.* **123**, 137602 (2019).

58. G. P. Vacca, L. Zambelli, Multimeson Yukawa interactions at criticality. *Phys. Rev. D* **91**, 125003 (2015).

59. L. Wang, P. Corboz, M. Troyer, Fermionic quantum critical point of spinless fermions on a honeycomb lattice. *New J. Phys.* **16**, 103008 (2014).

60. Z.-X. Li, Y.-F. Jiang, H. Yao, Fermion-sign-free Majarana-quantum-Monte-Carlo studies of quantum critical phenomena of Dirac fermions in two dimensions. *New J. Phys.* **17**, 085003 (2015).

61. S. Hesselmann, S. Wessel, Thermal ising transitions in the vicinity of two-dimensional quantum critical points. *Phys. Rev. B* **93**, 155157 (2016).

62. Z.-X. Li, Z.-Q. Wan, H. Yao, Asymptotic sign free in interacting fermion models. arXiv:2211.00663 [cond-mat.str-el] (2022).

63. C. Feng, E. Ibarra-García-Padilla, K. R. A. Hazzard, R. Scalettar, S. Zhang, E. Vitali, Metal-insulator transition and quantum magnetism in the SU(3) fermi-Hubbard model. *Phys. Rev. Res.* **5**, 043267 (2023).

64. E. Ibarra-García-Padilla, C. Feng, G. Pasqualetti, S. Fölling, R. T. Scalettar, E. Khatami, K. R. A. Hazzard, Metal-insulator transition and magnetism of SU(3) fermions in the square lattice. *Phys. Rev. A* **108**, 053312 (2023).

65. H. Ozawa, S. Taie, Y. Takasu, Y. Takahashi, Antiferromagnetic spin correlation of SU(N) fermi gas in an optical superlattice. *Phys. Rev. Lett.* **121**, 225303 (2018).

66. S. Taie, E. Ibarra-García-Padilla, N. Nishizawa, Y. Takasu, Y. Kuno, H. T. Wei, R. T. Scalettar, K. R. A. Hazzard, Y. Takahashi, Observation of antiferromagnetic correlations in an ultracold SU(N) Hubbard model. *Nat. Phys.* **18**, 1356–1361 (2022).

67. T. C. Lang, Z. Y. Meng, A. Muramatsu, S. Wessel, F. F. Assaad, Dimerized solids and resonating plaquette order in SU(N)-Dirac fermions. *Phys. Rev. Lett.* **111**, 066401 (2013).

68. Z. Zhou, D. Wang, Z. Y. Meng, Y. Wang, C. Wu, Mott insulating states and quantum phase transitions of correlated SU(2N) Dirac fermions. *Phys. Rev. B* **93**, 245157 (2016).

69. Y.-Y. He, H. Q. Wu, Y. Z. You, C. Xu, Z. Y. Meng, Z. Y. Lu, Quantum critical point of Dirac fermion mass generation without spontaneous symmetry breaking. *Phys. Rev. B* **94**, 241111 (2016).

70. Z.-X. Li, Y.-F. Jiang, S.-K. Jian, H. Yao, Fermion-induced quantum critical points. *Nat. Commun.* **8**, 314 (2017).

71. H. Xu, X. Li, Z. Zhou, X. Wang, L. Wang, C. Wu, Y. Wang, Trion states and quantum criticality of attractive SU(3) Dirac fermions. *Phys. Rev. Res.* **5**, 023180 (2023).

72. M. Gell-Mann, Symmetries of baryons and mesons. *Phys. Rev.* **125**, 1067–1084 (1962).

73. B. Rosenstein, H.-L. Yu, A. Kovner, Critical exponents of new universality classes. *Phys. Lett. B* **314**, 381–386 (1993).

74. L. Janssen, I. F. Herbut, Antiferromagnetic critical point on graphene's honeycomb lattice: A functional renormalization group approach. *Phys. Rev. B* **89**, 205403 (2014).

75. S. R. White, D. J. Scalapino, R. L. Sugar, E. Y. Loh, J. E. Gubernatis, R. T. Scalettar, Numerical study of the two-dimensional Hubbard model. *Phys. Rev. B* **40**, 506–516 (1989).

76. E. S. Sørensen, M. Wallin, S. M. Girvin, A. P. Young, Universal conductivity of dirty bosons at the superconductor-insulator transition. *Phys. Rev. Lett.* **69**, 828–831 (1992).

77. Y.-R. Shu, S. Yin, D.-X. Yao, Universal short-time quantum critical dynamics of finite-size systems. *Phys. Rev. B* **96**, 094304 (2017).

78. Y.-R. Shu, S.-K. Jian, S. Yin, Nonequilibrium dynamics of deconfined quantum critical point in imaginary time. *Phys. Rev. Lett.* **128**, 020601 (2022).

79. Y. Otsuka, S. Yunoki, S. Sorella, Universal quantum criticality in the metal-insulator transition of two-dimensional interacting Dirac electrons. *Phys. Rev. X* **6**, 011029 (2016).

80. T. C. Lang, A. M. Läuchli, Chiral Heisenberg Gross-Neveu-Yukawa criticality: Honeycomb vs. SLAC fermions. arXiv:2503.15000 [cond-mat.str-el] (2025).

81. N. Read, S. Sachdev, Valence-bond and spin-Peierls ground states of low-dimensional quantum antiferromagnets. *Phys. Rev. Lett.* **62**, 1694–1697 (1989).

82. N. Read, S. Sachdev, Spin-Peierls, valence-bond solid, and Néel ground states of low-dimensional quantum antiferromagnets. *Phys. Rev. B* **42**, 4568–4589 (1990).

83. Y. Da Liao, X. Y. Xu, Z. Y. Meng, Y. Qi, Dirac fermions with plaquette interactions. ii. SU(4) phase diagram with Gross-Neveu criticality and quantum spin liquid. *Phys. Rev. B* **106**, 115149 (2022).

84. D. Wang, Y. Li, Z. Cai, Z. Zhou, Y. Wang, C. Wu, Competing orders in the 2D half-filled SU(2*n*) Hubbard model through the pinning-field quantum Monte Carlo simulations. *Phys. Rev. Lett.* **112**, 156403 (2014).

85. Z. Zhou, C. Wu, Y. Wang, Mott transition in the π-flux SU(4) Hubbard model on a square lattice. *Phys. Rev. B* **97**, 195122 (2018).

86. X. Y. Xu, Y. Qi, L. Zhang, F. F. Assaad, C. Xu, Z. Y. Meng, Monte Carlo study of lattice compact quantum electrodynamics with fermionic matter: The parent state of quantum phases. *Phys. Rev. X* **9**, 021022 (2019).

87. W. Wang, D.-C. Lu, X. Y. Xu, Y.-Z. You, Z. Y. Meng, Dynamics of compact quantum electrodynamics at large fermion flavor. *Phys. Rev. B* **100**, 085123 (2019).

88. L. Janssen, W. Wang, M. M. Scherer, Z. Y. Meng, X. Y. Xu, Confinement transition in the QED_3-Gross-Neveu-XY universality class. *Phys. Rev. B* **101**, 235118 (2020).

89. S. Han, I. F. Herbut, Gross-Neveu-Yukawa theory of SO(2*n*)→SO(*n*)×SO(*n*) spontaneous symmetry breaking. *Phys. Rev. B* **110**, 125131 (2024).

90. S. Ray, Unconventional Gross-Neveu quantum criticality: Interaction-induced SO(3)-biadjoint insulator and emergent SU(3) symmetry. *Phys. Rev. B* **109**, 165137 (2024).

91. S. Han, S. Ray, I. F. Herbut, Gross-Neveu-Yukawa SO(2) and SO(3) tensorial criticality. *Phys. Rev. B* **111**, 115131 (2025).